β-decay half-lives and β-delayed neutron emission probabilities of nuclei in the region $A \lesssim 110$, relevant for the r process

J. Pereira,[1,2,*] S. Hennrich,[2,3,4] A. Aprahamian,[5,6] O. Arndt,[3,4] A. Becerril,[1,2,7] T. Elliot,[1,2,7] A. Estrade,[1,2,7] D. Galaviz,[1,2,†] R. Kessler,[2,3,4] K.-L. Kratz,[4,8] G. Lorusso,[1,2,7] P. F. Mantica,[1,9] M. Matos,[1,2] P. Möller,[10] F. Montes,[1,2] B. Pfeiffer,[3,4] H. Schatz,[1,2,7] F. Schertz,[2,3,4] L. Schnorrenberger,[2,11] E. Smith,[2,12] A. Stolz,[1] M. Quinn,[5,6] W. B. Walters,[13] and A. Wöhr[5,6]

[1]*National Superconducting Cyclotron Laboratory, Michigan State University, East Lansing, Michigan, USA*

[2]*Joint Institute for Nuclear Astrophysics, Michigan State University, East Lansing, Michigan, USA*

[3]*Institut für Kernchemie, Universität Mainz, Mainz, Germany*

[4]*Virtuelles Institut für Struktur der Kerne and Nuklearer Astrophysik, Mainz, Germany*

[5]*Institute of Structure and Nuclear Astrophysics, University of Notre Dame, South Bend, Indiana, USA*

[6]*Joint Institute for Nuclear Astrophysics, University of Notre Dame, South Bend, Indiana, USA*

[7]*Department of Physics and Astronomy, Michigan State University, East Lansing, Michigan, USA*

[8]*Max Planck Institut für Chemie, Otto-Hahn-Institut, Mainz, Germany*

[9]*Department of Chemistry, Michigan State University, East Lansing, Michigan, USA*

[10]*Theoretical Division, Los Alamos National Laboratory, New Mexico, USA*

[11]*Institut für Kernphysik, TU Darmstadt, Darmstadt, Germany*

[12]*Department of Physics, Ohio State University, Columbus, Ohio, USA*

[13]*Department of Chemistry and Biochemistry, University of Maryland, College Park, Maryland, USA*

(Received 30 December 2008; published 26 March 2009)

Measurements of β-decay properties of $A \lesssim 110$ r-process nuclei have been completed at the National Superconducting Cyclotron Laboratory at Michigan State University. β-decay half-lives for ^{105}Y, ^{106,107}Zr, and ^{111}Mo, along with β-delayed neutron emission probabilities of ^{104}Y, ^{109,110}Mo and upper limits for ^{105}Y, $^{103-107}$Zr, and ^{108,111}Mo have been measured for the first time. Studies on the basis of the quasi-random-phase approximation are used to analyze the ground-state deformation of these nuclei.

DOI: 10.1103/PhysRevC.79.035806 PACS number(s): 23.40.−s, 21.10.Tg, 27.60.+j, 26.30.−k

I. INTRODUCTION

The rapid neutron-capture process (r process) [1,2] remains as one of the most exciting and challenging questions in nuclear astrophysics. In particular, the theoretical quest to explain the production of r-process isotopes and the astrophysical scenario where this process occurs have not yet been satisfactorily solved (for a general review see, for instance, Refs. [3–5]). R-process abundance distributions are typically deduced by subtracting the calculated s- and p-process contributions from the observed solar system abundances. Furthermore, elemental abundances originated in the early galaxy can be directly observed in metal-poor, r-process-enriched stars (MPRES) (i.e., [Fe/H] $\lesssim -2$, [Ba/Eu] $\lesssim -0.7$, [Eu/Fe] $\gtrsim +1$). These combined observations reveal disparate behavior for light and heavy nuclei: MPRES abundance patterns are nearly consistent from star to star and with the relative solar system r-process abundances for the heavier neutron-capture elements $A \gtrsim 130$ (Ba and above), suggesting a rather robust main r process operating over the history of the galaxy. Such a consistent picture is not seen for light neutron-capture elements in the range $39 \leqslant Z \leqslant 50$, as the solar system Eu-normalized elemental abundances in MPRES show a scattered pattern [6–9]. Anticorrelation trends between elemental abundances and Eu richness at different metalicities have been suggested to provide a hint for an additional source of isotopes below $A \simeq 130$ [10–14]. Measured abundances of ^{107}Pd and ^{129}I, for $A < 130$, and ^{182}Hf, for $A > 130$, trapped in meteorites in the early solar system formation [15,16], further reinforce the idea of different origins for isotopes lighter and heavier than $A = 130$ (see, e.g., Ref. [17]).

Reliable nuclear physics properties for the extremely neutron-rich nuclei along the r-process path are needed to interpret the observational data in the framework of proposed astrophysical models. The r-process abundance region around $A \simeq 110$, prior to the $A = 130$ peak, is one region of intense interest, where the astrophysical models underestimate the abundances by an order of magnitude or more. It has been shown that the underproduction of abundances can be largely corrected under the assumption of a reduction of the $N = 82$ shell gap far from stability [19–22]. Whereas such quenching effect was suggested in elements near Sn—via analysis of the β decay of ^{130}Cd into ^{130}In [23]—its extension toward lighter isotones $^{129}_{47}\mathrm{Ag}_{82}$, $^{128}_{46}\mathrm{Pd}_{82}$ and below would have crucial consequences in the search for the r-process site. In this sense, self-consistent mean-field model calculations predict that the $N = 82$ shell quenching might be associated with the emergence of a harmonic-oscillator-like doubly semimagic nucleus $^{110}_{40}\mathrm{Zr}_{70}$, arising from the weakening of the energy potential surface due to neutron skins [24–27]. Thus, it is imperative to characterize the evolution of nuclear shapes in the region of ^{110}Zr.

*pereira@nscl.msu.edu

†Present address: Centro de Física Nuclear da Universidade de Lisboa, 1649-003, Lisboa, Portugal.

The goal of the experiment reported here was to use measured β-decay properties of nuclei in the neighborhood of ^{110}Zr to investigate its possible spherical character arising from new semimagic numbers [24,25] or even a more exotic tetrahedral-symmetry type predicted by some authors [28,29]. In particular, the measured half-lives ($T_{1/2}$) and β-delayed neutron-emission probabilities (P_n) can be used as first probes of the structure of the β-decay daughter nuclei in this mass region, where more detailed spectroscopy is prohibitive because of the low production rates at present radioactive beam facilities. A similar approach has already been used [30–37]. In addition to the nuclear-structure interest, our measurements also serve as important direct inputs in r-process model calculations. The $T_{1/2}$ values of r-process waiting-point nuclei determine the pre freeze-out isotopic abundances and the speed of the process toward heavier elements. The P_n values of r-process isobaric nuclei define the decay path toward stability during freeze-out and provide a source of late-time neutrons.

In the present article, the measurements of $T_{1/2}$ and P_n of $^{100-105}$Y, $^{103-107}$Zr, $^{106-109}$Nb, $^{108-111}$Mo, and $^{109-113}$Tc are reported. The work is contextualized amid a series of β-decay r-process experimental campaigns, carried out at the National Superconducting Cyclotron Laboratory (NSCL) at Michigan State University (MSU). Details of the experiment setup and measurement techniques are provided in Sec. II, followed by a description of the data analysis in Sec. III. The results are further discussed in Sec. IV on the basis of the quasi-random-phase approximation (QRPA) [38–41] using nuclear shapes derived from the finite-range droplet model (FRDM) [42] and the latest version of the finite-range liquid-drop model (FRLDM) [43,44]. The article closes with the presentation of the main conclusions and future plans motivated by the current measurements.

II. EXPERIMENT

A. Production and separation of nuclei

Neutron-rich Y, Zr, Nb, Mo, and Tc isotopes were produced by fragmentation of a 120-MeV/u ^{136}Xe beam in a 1242 mg/cm^2 Be target. The primary beam was produced at the NSCL Coupled Cyclotrons [45] at an average intensity of 1.5 pnA ($\sim 1 \times 10^{10}$ s^{-1}). Forward-emitted fragmentation reaction products were separated in-flight with the A1900 fragment separator [46]—operated in its achromatic mode—using the $B\rho$-ΔE-$B\rho$ technique [47]. Two plastic scintillators located at the intermediate (dispersive) focal plane and at the experimental area were used to measure the time-of-flight (TOF), related to the velocity of the transmitted nuclei. The first of these scintillators provided also the transversal positions x_d of the transmitted nuclei at the dispersive plane. A Kapton wedge was mounted behind this detector to keep the achromatism of the A1900. Energy losses experienced by nuclei passing through this degrader system of 22.51 mg/cm^2 (Kapton) and 22.22 mg/cm^2 (BC400) thickness provided a further filter to select a narrower group of elements. A total of 29 neutron-rich isotopes ($^{100-105}$Y, $^{102-107}$Zr, $^{104-109}$Nb, $^{106-111}$Mo, and $^{109-113}$Tc) defined the cocktail beam that was transmitted to the implantation station.

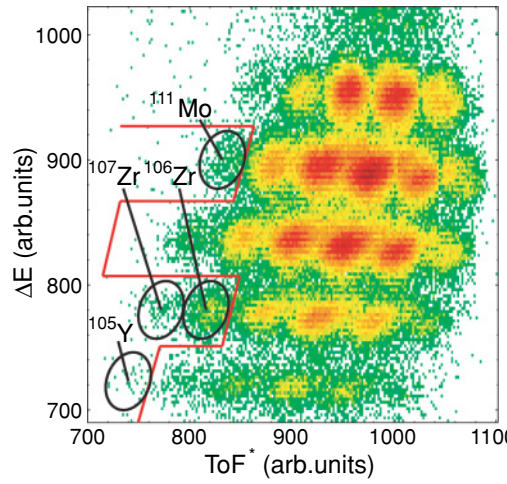

FIG. 1. (Color online) Particle-identification (PID) spectra collected during 112 hours of beam time, showing the different nuclei characterizing the cocktail beam transmitted to the end station. The solid line marks the r-process region of interest (left side). The r-process waiting-point nuclei analyzed in the present experiment are indicated by the ellipses.

The trajectory followed by the nuclei at the A1900 dispersive focal plane depended on their magnetic rigidities $B\rho$, which, in turn, were related to the corresponding velocities and mass-over-charge ratios. An event-by-event separation of the transmitted nuclei according to their mass A and proton Z numbers was achieved by combining the measured TOF and x_d with the energy-loss ΔE in a silicon PIN detector located in the implantation station. The latter quantity had to be corrected from its velocity dependence (described by the Bethe-Bloch equation [48]). The identification of nuclei transmitted through the A1900 is shown in Fig. 1. In this figure, the variable TOF* corresponds to the TOF corrected from its x_d dependence.

The maximum 5% $B\rho$ acceptance of the A1900 included the nuclei of interest, along with three primary-beam charge states ^{136}Xe^{+51}($B\rho = 3.8251$ Tm), ^{136}Xe^{+50}($B\rho =$ 3.9016 Tm), and ^{136}Xe^{+49}($B\rho = 3.9812$ Tm), with particle rates of 8.7×10^6 s^{-1}, 3.5×10^4 s^{-1}, and 80 s^{-1}, respectively. As these contaminants could reach the intermediate image plane, resulting in the damage of the plastic scintillator, it was necessary to stop them with the standard A1900 slits and a 17.4-mm-wide tungsten finger located in the first image plane. This slit configuration blocked the most intense contaminants with a minor reduction of the $B\rho$ acceptance of the fragments of interest. Thus, the ^{136}Xe^{+50} charge state was blocked by the finger at the central position of the transversal plane, while ^{136}Xe^{+51} stopped in one of the slits, closed at 39.88 mm from the optical axis (in the low-$B\rho$ side). The high-$B\rho$ slit was fully opened so that the fragment of interest (along with the low-intensity contaminant ^{136}Xe^{+49}) were transmitted through the second half of the A1900. The resulting overall $B\rho$ acceptance was about 4%.

B. Implantation station

Nuclei transmitted through the A1900 and beam transport system were implanted in the NSCL β counting system (BCS) [49] for subsequent analysis. The BCS consisted of a stack of four silicon PIN detectors (PIN1–4) of total thickness 2569 μm, used to measure the energy loss of the exotic species, followed by a 979-μm-thick 40×40-pixel double-sided silicon strip detector (DSSD) wherein implanted nuclei were measured along with their subsequent position-correlated β decays. Located 9 mm downstream of the DSSD, a 988-μm-thick 16-strip single-sided Si detector (SSSD) and a 10-mm-thick Ge crystal, separated 2 mm from each other, were used to veto particles whose energy loss in the DSSD was similar to that left by β decays. The signals from each DSSD and SSSD strip were processed by preamplifiers with high- and low-gain outputs, each defined over a scale-range equivalent to 100 MeV and 3 GeV, respectively. Energy thresholds for the low-gain signals were set to values around 300 MeV. High-gain signals from every DSSD and SSSD strips were energy matched in the beginning of the experiment using a ^{228}Th α source as reference, whereas independent threshold were adjusted using a ^{90}Sr β source. Two of the DSSD strips (the front-side 31st and the back-side 12th) were damaged and consequently had to be disabled during the experiment, raising their high/low-gain thresholds to maximum values. Energy thresholds for the PIN detector were set to 2000 MeV for the first detector and around 300 MeV for the rest of PIN detectors. A dedicated unwedged setting of the A1900, transmitting a large amount of light fragments, was used in the beginning of the experiment to energy-calibrate the PIN detectors and low-gain signals from DSSD. The measured energy losses were compared with calculations performed with the LISE program [50], using the Ziegler energy-loss formulation [51].

The BCS was surrounded by the neutron emission ratio observer (NERO) detector [52–54], which was used to measure β-delayed neutrons in coincidence with the β-decay precursor. This detector consisted of 60 (16 ^{3}He and 44 B_3F) proportional gas-counter tubes, embedded in a $60 \times 60 \times 80$ cm^3 polyethylene moderator matrix. The detectors were set parallel to the beam direction and arranged in three concentric rings around a 22.4-cm-diameter vacuum beam line that accommodated the BCS. β-delayed neutrons were thermalized in the polyethylene moderator to maximize the neuron capture cross section in the ^{3}He and B_3F gas counters. Gains and thresholds of the neutron counters were adjusted using a ^{252}Cf postfission neutron source.

The master-event trigger was provided by the PIN1 detector or by a coincidence between the DSSD front and back high-gain outputs. The master trigger opened a 200-μs time window [37,54], during which signals from the NERO counters were recorded by an 80 ms-range multihit TDC. The 200-μs interval was chosen on the basis of an average moderation time of about 150 μs, measured for neutrons emitted from a ^{252}Cf source. Energy signals of moderated neutrons were also collected in an ADC. The closure of the time window was followed by the readout of the BCS and NERO electronics.

C. Identification of nuclei

The particle identification (PID) was performed with a dedicated setup installed upstream of the BCS/NERO end station. Several nuclei having μs isomers with known γ-decay transitions were selected in a specific A1900 setting and implanted in a 4-mm-thick aluminum foil, surrounded by three γ-ray detectors from the MSU segmented germanium array (SeGA) [55]. These detectors were energy and efficiency calibrated using sources of ^{57}Co, ^{60}Co, and ^{152}Eu. The γ-peak efficiency was about 6% at 1 MeV. A 50×50 mm^2, 503 μm-thick silicon PIN detector (PIN0) upstream of the aluminium foil was used to measure ΔE, which, combined with TOF and x_d, allowed for an identification of the various nuclei transmitted in the setting according to their Z and A numbers. The measurement of these three signals, gated in specific known isomeric γ-decay lines, provided a filter to identify the corresponding μs isomers.

Four settings of the A1900 were used to identify the nuclei of interest in a stepwise fashion based on the observation of the μs isomers. In each of these settings, the first half of the A1900 was tuned to $B\rho = 3.9016$ Tm—defined by the rigidities of the nuclei of interest—while the second half was tuned to $B\rho = 3.7881$ Tm, $B\rho = 3.7929$ Tm, $B\rho = 3.7976$ Tm, and $B\rho = 3.8024$ Tm. The four values were chosen to have fragments transmitted in two consecutive settings, and far enough to cover the entire range of rigidities of interest. In the first setting $B\rho = 3.7881$ Tm, several γ lines were seen for the μs-isomeric states of ^{121}Pd (135 keV), ^{123}Ag (714 keV), ^{124}Ag (156 keV), ^{125}Ag (684 keV), and ^{125}Cd (720 keV and 743 keV) [56,57]. From these references, it was possible to identify the more exotic nuclei present in the subsequent settings. The particle identification was further confirmed by detecting the 135-keV γ line from the isomer ^{121}Pd transmitted in the settings $B\rho = 3.7929$ Tm and $B\rho = 3.7976$ Tm. The fourth setting $B\rho = 3.8024$ Tm was chosen to optimize the transmission of the nuclei of interest to the final end station. After the PID was completed, the Al catcher and PIN0 detector were retracted. The cocktail beam was then transmitted to the final BCS/NERO end station, where the ΔE necessary for the PID spectrum was provided by the PIN1 detector.

The PID spectrum shown in Fig. 1 includes the fully stripped ions of the nuclei of interest, overlapped with a small fraction of charge states contaminants from lighter isotopes. Given the high $B\rho$ selected in the A1900 setting, only the hydrogen-like ions with mass numbers $A - 2$ and $A - 3$ reached the experimental area. These contaminants were disentangled from the fully stripped nuclei by measuring the total kinetic energy (TKE) of the transmitted ions compiled from signals of the PIN detectors and DSSD. The TKE spectra of different Zr isotopes is shown in Fig. 2: the upper row of panels corresponds to the nuclei that were detected with the first PIN detector of the BCS. The double-peak structure in the TKE spectra arises from the fully stripped species (high-TKE peak) and the corresponding hydrogen-like contaminants (low-TKE peak). The central and lower row of panels show the same spectra with the additional requirement of being implanted in either the most downstream PIN detector

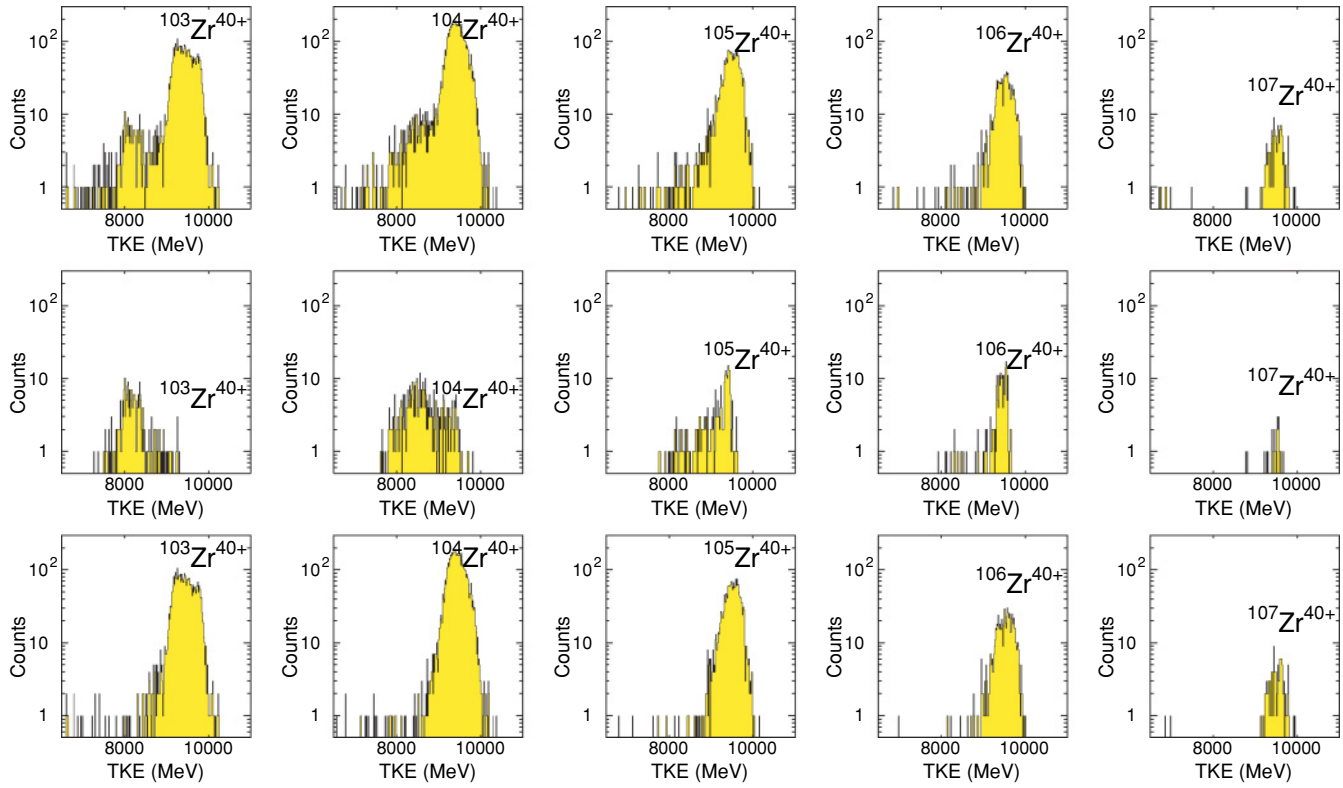

FIG. 2. (Color online) Total kinetic energy (TKE) of Zr isotopes identified in the PID spectrum. The different spectra rows correspond to all detected events in PIN1 (upper row), nuclei that were implanted in PIN4 (central row), and nuclei that were implanted in DSSD (lower row). The fully stripped ions are labeled on top of the corresponding high-TKE peaks.

in the stack (i.e., PIN4) (central row) or in the DSSD (lower row). Nearly only the fully stripped nuclei reached the latter, whereas the hydrogen-like components were mainly implanted in the last PIN. A small fraction of the fully stripped components did not reach the DSSD due to a slightly overestimated Si thickness. Furthermore, no low-gain signals from the SSSD were observed, demonstrating that no nuclei reached this detector.

III. DATA ANALYSIS

A. β-decay half-lives

Specific conditions in the different detectors of the BCS were required to distinguish implantations, decays, and light-particle events: a signal registered in each of the four PIN detectors, in coincidence with the low-gain output from at least one strip on each side of the DSSD, and in anticoincidence with the SSSD, was identified as an implantation event. Decay events were defined as high-gain output signals from at least one strip on each side of the DSSD, in anticoincidence with signals from PIN1. Software thresholds were set separately for each DSSD strip to cut off noise. Decaylike events accompanied by a preamplifier overflow signal from the Ge crystal downstream of the DSSD were identified as light particles and consequently rejected. According to LISE-based calculations, these light particles were mainly tritium nuclei and, to a lesser degree, ^{8}Li nuclei, with energy-loss signals in the DSSD high-gain output comparable to the decays of interest.

For each implantation event, the strip location on each side of the DSSD—defining the implanted pixel—was determined from the average of the strips weighted by their respective energy signal amplitude. The resulting average pixel was recorded along with the implantation time taken from a continuously counting 50-MHz clock. The last beam-line quadrupoles in front of the BCS were adjusted to illuminate a wide area of the DSSD cross section; the resulting distribution of implantation events is shown in Fig. 3. Subsequent decay events occurring in the same or neighboring pixels (defining a cluster of nine pixels) within a give correlation-time window (t_c) were associated with the previous implantation, and their times and pixels recorded. The value of t_c was chosen to be around 10 times the expected $T_{1/2}$. Whenever a decaylike event was correlated with more than one implantation, all the events within the sequence (i.e., decay and implantations) were rejected. Such scenario would be possible if different implantations occur in the same cluster within the correlation-time window. Given the low maximum implantation rate per pixel of about 1.8×10^{-3} s^{-1} and the $T_{1/2}$ values (typically below 1 s), the probability of multiple implantation events correlated with a decay was negligible.

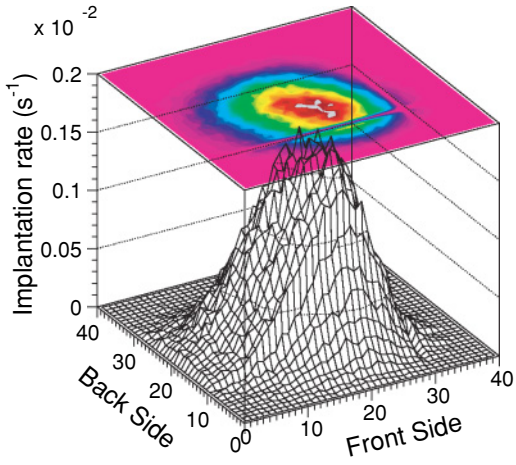

FIG. 3. (Color online) Implantation-event distribution measured over 112 hours of beam on target. The damaged 12th back strip and 31st front strip in the DSSD can be observed as respective gaps on the top-plane projection.

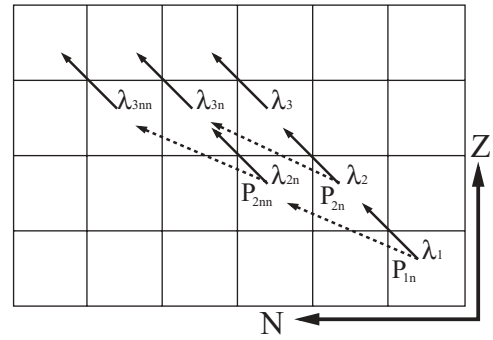

FIG. 4. Schematic representation of the possible decay paths followed by a decaying mother nucleus (1), including first (2) and second (3) descendant-nuclei generations. Solid lines correspond to direct β-decay paths; dashed lines correspond to β-delayed neutron-emission paths. (See text for details).

1. β-decay background

The implantation-decay correlation criterion did not prevent the occurrence of spurious correlations arising from sources other than the actual decays of interest. Possible background sources included the following: light particles that did not lead to overflows in the Ge detector (either because they missed the detector or because they deposited only a fraction of their energy), real decays from longer-lived implanted nuclei and from nuclei implanted in neighboring pixels, and electronic noise signals above the thresholds. A detailed study of this decaylike background was necessary to extract $T_{1/2}$ values.

Background rates were determined separately for each DSSD cluster and 1-h data-collection run, counting the number of decaylike events that were not correlated with any implantation. During this background measurement, each time an implantation was detected in a given pixel, the corresponding 9-pixel cluster was blocked to any subsequent decay event during a time interval chosen to be longer than t_c. Decaylike events detected in that cluster after the closure of the postimplantation blocking time (i.e., those that were not correlated with the previous implantation) were recorded as background events. Background rates were calculated for each 1-h run as the ratio of the number of uncorrelated decay events in each cluster to the unblocked time in that cluster. The resulting rates were position dependent and nearly constant over different runs. A critical factor in this analysis was the length of the postimplantation blocking time which had to be chosen so as to minimize the probability of recording real correlated decays. A blocking-time window of 40 s was found to fulfill this requirement. Finally, the DSSD cluster-averaged β-decay background was about 0.01 s^{-1}, nearly constant throughout the experiment.

The total number of β-decay background events B_β for each isotope was calculated from the measured background rates in the runs and pixels where the isotopes were implanted, multiplied by t_c. The background rate for a given nucleus was given by B_β, divided by the total blocking time (calculated as the product of the number of implantations and t_c). The statistical error for the background rate of each nucleus, derived from the number of background events recorded in each DSSD cluster and run, was about 5%.

2. β-decay half-lives from decay-curve fits

The time differences between implantation and correlated decay events were accumulated for each nucleus in separated histograms and fitted by least-squares to a multiparameter function derived from the Batemann equations [58]. Due to the limited detection efficiency of the DSSD, some of the recorded β-decay events may come from descendant nuclei following a missed decay of the nuclei of interest. Given the low probability of missing consecutive decays, the correlation times used in the analysis, and the values of the half-lives of the descendant nuclei, up to three generations were included in the fit functions, along with contributions from background events. The paths that define the possible decay sequences following the decay of a mother nucleus are schematically illustrated in Fig. 4.

The fit equation included a total of 11 parameters, 8 of them fixed to constant values, namely the decay constants of the daughter (λ_2) and granddaughter (λ_3); the neutron-emission probability of the mother (P_{1n}), daughter (P_{2n}), and neutron-emitted daughter (P_{2nn}); and the decay constants of the single neutron-emitted daughter (λ_{2n}) and granddaughter (λ_{3n}) and the double neutron-emitted granddaughter (λ_{3nn}). These fit constants were taken from the literature or, in the case of some unknown P_{1n}, calculated using the FRDM+QRPA model [39–42]. The remaining three parameters were treated as free variables to be determined from the fit algorithm; two of them were the decay constant of the mother nucleus (λ_1) and the initial number of mother decaying nuclei (N_0). The third parameter, namely the background constant, was treated as a constrained "free" variable, defined within ±10% of the calculated value (see Sec. III A1). Finally, after determining the P_n as described in Sec. III B, the decay curves were refitted replacing P_{1n} by the newly measured values. The decay curves

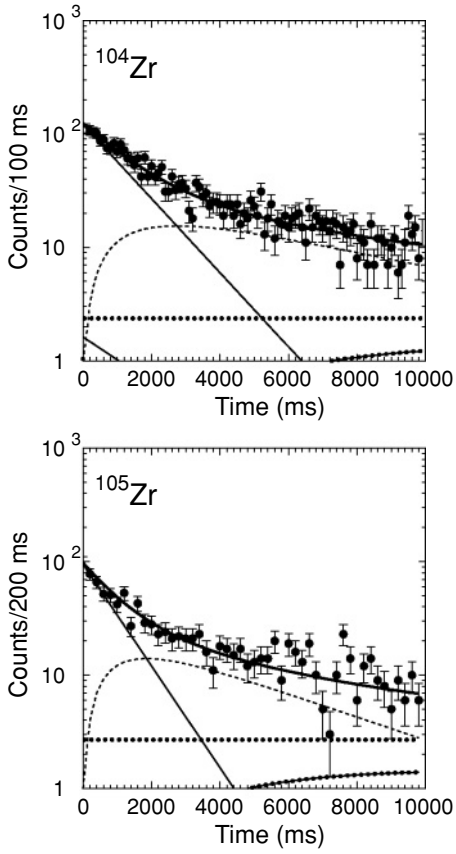

FIG. 5. Decay curve data (full circles) for $^{104,105}Zr_{64,65}$ isotopes. Included are fit functions for mother (solid thin line), daughter (dashed line), granddaughter (dot-dashed line), and background (dotted line). The sum of these functions is represented by the solid thick line.

of some selected Zr isotopes are presented in Fig. 5 with the different contributions to the total fit curve.

The least-squares method used to fit the decay-curve histograms requires that the number of events per bin size Δt is described by Gaussian statistics. More formally, the individual probability for one event to be recorded in a given bin must be $\ll 1$, and the total number of events per bin $N(\Delta t)$ must be large, typically ~ 20. Taking the time scale of the histograms as t_c, the latter condition can be expressed as $N(\Delta t) = (\Delta t/t_c)N \sim 20$, where N is the total number of decay events in the histogram. Thus, because $\Delta t/t_c \ll 1$, N must be $\gg 200$ for the least-squares method to be valid. Table I shows the half-lives of those nuclei that fulfilled the Gaussian statistics requirement, along with their corresponding N. For cases with lower statistics, an alternative analysis based on the maximum likelihood method was used (see Sec. III A3).

Different sources of systematic error were included in the decay-curve analysis: uncertainties in the input parameters (half-lives and neutron-emission probabilities of the descendant nuclei) were accounted for by comparing the fit results obtained with these input values scanned over their respective error intervals. The resulting errors depended on the half-lives of the mother and, to a lesser degree, descendant nuclei. Uncertainties were typically below 5%. In addition, comparisons of fit half-lives using background rates varied over their corresponding uncertainty showed differences below 1%. Absolute systematic and statistical errors are shown in Table I.

3. *β-decay half-lives from maximum likelihood method*

The maximum likelihood analysis (MLH) is well suited for determining decay half-lives in cases with low statistics [37,71–76]. The method, described in Appendix A, defines decay sequences for up to three generations following an implantation. The probability of observing a given decay sequence was calculated by summing up the probabilities for all possible scenarios leading to the detection of the decay-event members. The scenarios were evaluated by considering the occurrence of up to three β decay events, including β-delayed neutron branching, the contributions from background events, and the "missing" decays due to the limited detection efficiency. A joint probability density, the likelihood function $\mathcal{L}$, was calculated by multiplying the probabilities for all the measured decay sequences. The resulting $\mathcal{L}$ was a function of the measured decay times t_i of the different members of the decay sequence, their decay constants and neutron-emission probabilities, the correlation time t_c, the background rate of the corresponding DSSD cluster and run where the decay sequence was detected, and the β-decay detection efficiency ϵ_β. The half-lives of the nuclei of interest were determined from the maximization of $\mathcal{L}$, using the decay constant of the mother nucleus λ_1 as free parameter.

All of the descendant decay parameters necessary to define $\mathcal{L}$ were taken from previous measurements or—in the case few P_n values—calculated from theory. Similar to the least-squares fit method described in Sec. III A2, the half-lives were recalculated with the newly measured P_n values, once known. The β-decay detection efficiency ϵ_β was determined as the ratio of the number of detected β decays N_β attributed to a given nucleus to the number of implantations of that nucleus. The former was given by $N_\beta = N_0/(\lambda_1 \Delta t)$, where N_0 and λ_1 were obtained from the decay-curves fits, for the cases where the least-squares method was valid. No systematic trend for ϵ_β was observed within a given isotopic chain, so a weighted average efficiency per DSSD cluster of $(31 \pm 4)\%$ was used. Finally, the background rate was determined for each DSSD cluster and run, as described in Sec. III A1.

The sources of systematic error included contributions from uncertainties in the experimental descendant-nuclei $T_{1/2}$ and P_n, background and ϵ_β. The systematic error of $T_{1/2}$ was calculated for each nucleus as described in Sec. III A2, yielding typical values below 10%. The statistical error was directly calculated from the MLH analysis using the prescription described by W. Brüchle [77]. Because the $\mathcal{L}$ distributions were typically asymmetric, the shortest possible interval containing the maximum of the $\mathcal{L}$ distribution and 68% (i.e., 1-σ) of the total integrated density probability was used [37,77]. The calculated systematic and statistical uncertainties are listed in Table I. The total error shown in Fig. 6 was obtained summing up the contributions from systematic and statistical uncertainties according to the method described in Ref. [78]. The $T_{1/2}$ obtained from the MLH are in agreement with

TABLE I. Total number of implantations, number of events per histogram N, and experimental β-decay half-lives obtained from least-squares fit (Least-squares) and the maximum likelihood method (MLH) with systematic and statistical errors. The results are compared with available data from previous experiments (Literature) and with the versions QRPA03 and QRPA06 of Möller's QRPA model (see text for more details).

Isotope	Implantations	N	Half-life (ms)				
			Least-squares	MLH	Literature	QRPA03 [41]	QRPA06
^{100}Y	188	107		$660(25)^{+150}_{-120}$	940(32) [59], 735(7) [60]	349	291
^{101}Y	746	453		$510(30)^{+70}_{-60}$	450(20) [61]	194	138
^{102}Y	1202	976		410(20)(30)	300(10) [62], 360(40) [63]	107	176
^{103}Y	596	538		$260(10)^{+40}_{-30}$	230(20) [32]	87	80
^{104}Y	128	116		$260(10)^{+60}_{-50}$	180(60) [33]	32	28
^{105}Y	27	21		$160(15)^{+85}_{-60}$		48	43
^{103}Zr	2762	1842	1380(60)(40)	1320(90)(60)	1300(100) [64]	1948	1495
^{104}Zr	4743	3158	920(20)(20)	870(50)(30)	1200(300) [64]	1879	1358
^{105}Zr	1707	1118	670(20)(20)	$660(45)^{+50}_{-45}$	600(100) [32]	102	95
^{106}Zr	643	570		$260(20)^{+35}_{-30}$		381	261
^{107}Zr	90	91		$150(5)^{+40}_{-30}$		223	149
^{106}Nb	10445	8182	1240(15)(15)	1030(65)(30)	1020(50) [65]	191	142
^{107}Nb	6672	5384	290(10)(5)	280(15)(10)	330(50) [66]	777	452
^{108}Nb	1479	1731	210(2)(5)	220(10)(15)	193(17) [61]	468	229
^{109}Nb	268	340		130(5)(20)	190(30) [32]	461	281
^{108}Mo	17925	11732	1110(5)(10)	1020(65)(20)	1090(20) [67]	2168	1249
^{109}Mo	9212	7013	700(10)(10)	660(40)(20)	530(60) [68]	1989	869
^{110}Mo	2221	2453	340(5)(10)	330(20)(20)	270(10) [69]	1820	1144
^{111}Mo	167	210		$200(10)^{+40}_{-35}$		1189	699
^{109}Tc	2922	1623	1140(10)(30)	1040(95)(50)	860(40) [61]	378	338
^{110}Tc	9549	6256	910(10)(10)	820(50)(25)	920(30) [70]	321	242
^{111}Tc	5433	4626	350(10)(5)	350(15)(15)	290(20) [32]	191	185
^{112}Tc	1198	1206	290(5)(10)	290(10)(20)	280(30) [70]	159	216
^{113}Tc	84	80		$160(5)^{+50}_{-40}$	170(20) [33]	108	101

the decay-curve fits for the cases where the least-squares fit method was valid.

B. β-delayed neutron emission probabilities

The β decay of a neutron-rich nucleus can populate levels in the daughter nucleus above the neutron separation energy S_n, thus opening the β-delayed neutron-emission channel. The probability of observing a neutron associated with the β decay of a nucleus is given by the neutron-emission probability or P_n value (called P_{1n} in Sec. III A2). β-delayed neutrons were detected in coincidence with β decays using the NERO detector in conjunction with the BCS. P_n values were determined for each nucleus according to

$$P_n = \frac{N_{\beta n} - B_n - N_{\beta\beta n}}{\epsilon_n N_\beta}, \tag{1}$$

where $N_{\beta n}$ is the number of detected neutrons in coincidence with β decays correlated with previous implantations; B_n is the number of background β-neutron coincidences; ϵ_n is the neutron detection efficiency; and N_β is the number of β-decaying mother nuclei. $N_{\beta\beta n}$ is the number of detected β-delayed neutrons from descendant nuclei; it should be consequently subtracted from the total number of detected neutrons to determine the actual number of neutrons associated with the nucleus of interest. For the nuclear species discussed in this article, β-neutron coincidences associated with descendant nuclei other than the β-decay daughter were negligible. Using the Batemann equations [58], it is possible to write explicitly the value of $N_{\beta\beta n}$:

$$N_{\beta\beta n} = (1 - P_n)C, \tag{2}$$

where C is a constant given by:

$$C = \frac{\lambda_2 P_{nn} N_\beta \epsilon_n}{\lambda_2 - \lambda_1}\left[1 - e^{-\lambda_1 t_c} - \frac{\lambda_1}{\lambda_2}(1 - e^{-\lambda_2 t_c})\right]. \tag{3}$$

In this equation, P_{nn} is the neutron-emission probability of the daughter nucleus (called P_{2n} in Sec. III A2) and λ_2 and λ_1 are the decay constants of the daughter and mother nuclei, the latter being extracted from the analysis discussed in the previous sections. Inserting Eq. (2) and Eq. (3) into Eq. (1)

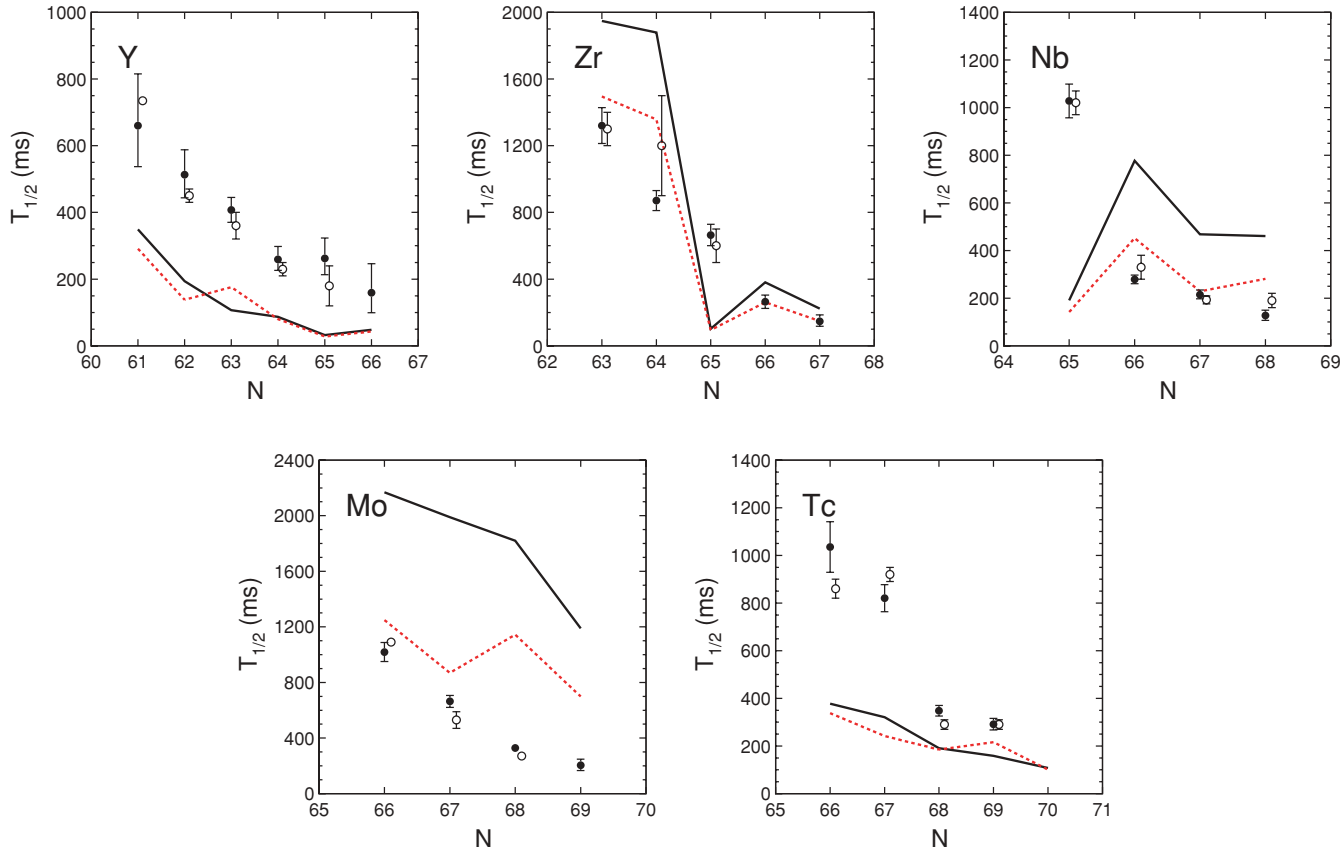

FIG. 6. (Color online) β-decay half-lives obtained from the maximum likelihood method for Y, Zr, Nb, Mo, and Tc isotopes (filled circles) compared with results from previous experiments [32,33,59–70] (open circles). For the sake of clarity, the latter were shifted to the right by 0.1 units. The data are compared with two versions of the QRPA model of Möller *et al.*: the version described in Ref. [41] (solid line) and the interim version QRPA06 described in Sec. IV A (dashed line) (see text for details).

and rearranging terms:

$$P_n = \frac{N_{\beta n} - B_n - C}{N_\beta \epsilon_n - C}. \tag{4}$$

The value of N_β for a given nucleus was calculated as the product of the total number of implantations by the average ϵ_β. The number of neutrons detected by NERO in coincidence with β decays were recorded in a multihit TDC. P_n values were first determined for the less exotic nuclei, taking λ_1 from Table I and λ_2 and P_{nn} from Ref. [61] (as their corresponding daughters were not included in the present experiment). The newly calculated values of P_n were then included in Eq. (4) as P_{nn} to calculate P_n for the next exotic nuclei.

1. *Neutron detection efficiency*

The design of the NERO detector was optimized to achieve a large and energy-independent efficiency, at least in the typical range of energies of the measured β-delayed neutrons. The efficiency response of NERO was determined at the Nuclear Structure Laboratory, at the University of Notre Dame, by detecting neutrons produced at different energies E_n from resonant and nonresonant reactions and from a ^{252}Cf source, as described in Ref. [54]. In that analysis, eight different values of E_n ranging from about 0.2 to 5 MeV were covered. The experimental results were extrapolated to a wider energy range, using the MCNP code [79]. The NERO efficiency is nearly constant for E_n below 0.5 MeV, and gradually decreases beyond this value, as discussed in Refs. [52,53]. Further analysis of the detector rings showed that, for energies below 1 MeV, where NERO is most efficient, the total efficiency was mainly governed by the innermost detector ring followed by the intermediate and external rings. This result suggested that, at those energies, the most efficient thermalization of neutrons takes place during the first interactions with the polyethylene moderator. Conversely, the three rings converge to nearly the same efficiency at energies above 1 MeV, where the total efficiency drops significantly (see Fig. 7).

In the present experiment, the energies of the β-delayed neutrons $E_{\beta n}$ ranged from zero to $Q_\beta - S_n$, where Q_β is the β-decay Q value of the mother nucleus and S_n is the neutron separation energy of the daughter nucleus. The distribution of $E_{\beta n}$ between these two values follows $\sim S_\beta(E) f(Q_\beta - E)$, where $S_\beta(E)$ is the β-decay strength function for a decay into the daughter's level at energy $E = S_n + E_{\beta n}$, and

$$f(Q_\beta - E) \sim (Q_\beta - S_n - E_{\beta n})^5. \tag{5}$$

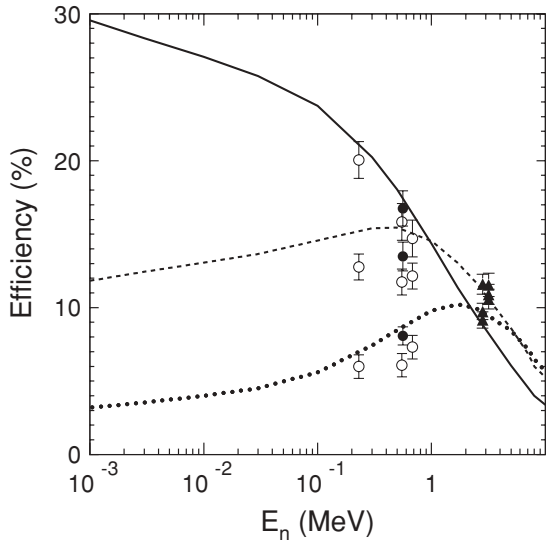

FIG. 7. MCNP-calculated efficiencies as a function of neutron energy E_n for the innermost ring (solid line), intermediate ring (dashed line), and external ring (dotted line) compared to the measured values from the reactions ^{11}B(α, n) (filled circles), ^{13}C(α, n) (triangles), and ^{51}V(p, n) (empty circles) and from a neutron postfission ^{252}Cf source (square). See Refs. [52,53] for more details.

The strong energy dependence of f largely favors S_β to excited levels of the daughter nucleus near its S_n. Moreover, as discussed in Refs. [80–82], high-resolution spectroscopic studies of β-delayed neutron-emitter nuclei produced by fission showed that $E_{\beta n}$ was always much lower than $Q_\beta - S_n$ (e.g., 199 keV for ^{87}Br, 450 keV for ^{98}Rb, and 579 keV for ^{137}I). This trend was also observed by the same authors in the total spectra of ^{235}U and ^{239}Pu, with average $E_{\beta n}$ of 575 and 525 keV, respectively, and with little neutron intensities at $E_{\beta n} \gtrsim 800$ keV [80,83]. The reason for these "compressed" $E_{\beta n}$ spectra is the strong, often preferred population of the lowest excited states in the final nuclei [82]. Because the region investigated in the present work includes strongly deformed nuclei, the respective expected low-laying excited states are rather low. Thus, it was safe to assume the $E_{\beta n}$ values of the nuclei of interest to be typically below 500 keV. For these low energies, a constant value of (37 $\pm$ 5)% for the NERO efficiency was assumed.

2. *Neutron background*

Free neutron background rates were independently recorded throughout the experiment using NERO in self-triggering mode. Four of these measurements were taken without beam, and two with beam on target. The background rates doubled from 4 to 8 s^{-1} when fragments were sent into the experimental setup, revealing the existence of two different background sources. The energy spectra recorded during the background measurements proved that the background origin could be attributed to actual neutrons. One of the neutron-background sources was intrinsic to the detector and its environment, whereas the other had a beam-linked origin. Analysis of the ring-counting ratios for background and production runs supported this idea (see Fig. 8). Measurements of β-delayed neutrons emitted from the implanted nuclei showed that the NERO counting rates were higher for the innermost ring (i.e., the closest to the DSSD) and systematically decreased for the next external rings. This results is compatible with MCNP simulations summarized in Fig. 7. Background runs with beam off showed the opposite trend, with high rates in the most external ring, which gradually decreased for the next internal ones. Such a result suggests that these runs were mainly affected by an external background source, most probably related to cosmic rays. Background runs with beam on target showed an intermediate situation that could be explained as arising from a combination of external and internal sources.

The value of B_n in Eq. (1) included contributions from neutron-β-background events (i.e., neutrons in coincidence with β-decay background events) $B_n(B_\beta)$, and from random coincidences between free NERO background events and real β decays $B_n(\beta)$. The value of $B_n(B_\beta)$ for each nucleus was calculated as the product of the neutron-β-background rate measured on each implanted DSSD cluster, and the neutron-detection time following the corresponding implantations of that nucleus. Because of the very low total number of neutron and β-decay background coincidences measured per DSSD cluster, the neutron-β-background rate on each cluster was determined by scaling the β-decay background rate calculated

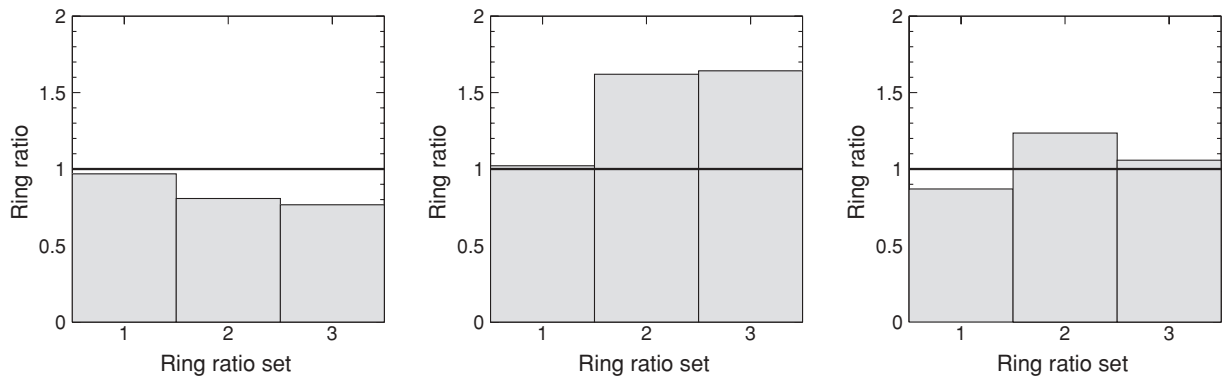

FIG. 8. Ratio of neutrons detected with different NERO rings for three different runs: production (left), background with beam off (center), and background with beam on (right). Histogram bin numbers 1, 2, and 3 correspond to ring ratios R_2/R_1, R_3/R_2, and R_3/R_1, where R_{1-3} are the innermost, intermediate, and external rings (see text for details).

TABLE II. P_n values obtained in the present experiment. The results are compared with available data from previous experiments (Literature) and with the versions QRPA03 and QRPA06 of Möller's QRPA model (see text for details).

Isotope	N_β	N_n	$B_n(B_\beta)$	$B_n(\beta)$	$P_n(\%)$			
					Present exp.	Literature	QRPA03 [41]	QRPA06
^{100}Y	58	1	0.4	0.1	$\leqslant$10	0.92(8) [61]	0.2	0.3
^{101}Y	231	3	0.6	0.4	$\leqslant$4	1.94(18) [61]	0.6	1.3
^{102}Y	373	10	1.1	0.6	6(2)	4.9(12) [61]	3.4	1.6
^{103}Y	185	6	0.5	0.3	8(2)	8(3) [32]	4.0	4.1
^{104}Y	40	5	0.1	0.1	34(10)		4.8	3.9
^{105}Y	8	1	0.03	0.01	$\leqslant$82		22.4	17.0
^{103}Zr	856	5	2.4	1.4	$\leqslant$1		0.0	0.0
^{104}Zr	1470	10	4.3	2.4	$\leqslant$1		0.0	0.0
^{105}Zr	529	4	1.5	0.8	$\leqslant$2		0.0	0.0
^{106}Zr	199	4	0.5	0.3	$\leqslant$7		0.7	0.7
^{107}Zr	28	1	0.04	0.04	$\leqslant$23		0.6	2.1
^{106}Nb	3238	70	9.1	5.2	5(1)	4.5(3) [32]	0.3	0.2
^{107}Nb	2068	68	5.7	3.3	8(1)	6(2) [32]	4.4	3.7
^{108}Nb	458	15	1.3	0.7	8(2)	6.2(5) [32]	15.6	11.0
^{109}Nb	83	3	0.2	0.1	$\leqslant$15	31(5) [32]	13.6	26.0
^{108}Mo	5557	35	24.2	8.9	$\leqslant$0.5		0.0	0.0
^{109}Mo	2856	27	8.1	4.6	1.3(6)		0.0	0.0
^{110}Mo	689	8	1.9	1.1	2.0(7)		0.0	0.0
^{111}Mo	52	1	0.1	0.1	$\leqslant$12		0.0	0.1
^{109}Tc	906	6	2.6	1.4	$\leqslant$1	0.08(2) [32]	0.0	0.0
^{110}Tc	2960	14	8.5	4.7	$\leqslant$4	0.04(2) [32]	0.2	0.1
^{111}Tc	1684	12	4.7	2.7	$\leqslant$1	0.85(20) [32]	0.4	0.6
^{112}Tc	371	6	0.5	0.6	4(1)	1.5(5) [33]	0.9	0.8

in Sec. III A1. The corresponding scaling factor, calculated as the DSSD cluster-averaged ratio of neutron-β-background coincidences to β-decay background events, was about 0.08 and nearly constant throughout the experiment. In addition to this background source, $B_n(\beta)$ was approximately calculated as the product of the number of mother β decays N_β, and the probability for at least one free neutron background with a rate 8 s^{-1} to be detected in random coincidence with a β decay. This latter approximation is not valid for coincidences of β decays with free background neutrons that were produced by fragmentation reactions induced by the same implanted mother nuclei. A calculated probability for this scenario, however, demonstrated that the occurrence of such a type of coincidences was negligible. Table II shows the value of N_β, N_n, $B_n(B_\beta)$, and $B_n(\beta)$.

3. *Error analysis*

The error analysis of P_n was derived from Eq. (4). In general, the main source came from uncertainties in the number of detected β-delayed neutrons $N_{\beta n}$ and background events, with typical values about 20% for each. The former had statistical origin, whereas the latter was calculated from the β-background uncertainties, described in Sec. III A1, and the error in the determination of the 0.08 scaling factor described in the previous section. An additional contribution of 15% to the total error came from uncertainties in the number of mother decays N_β, which were calculated by propagating the uncertainties in ϵ_β, according to Sec. III A3. Finally, an average 13.5% relative error in ϵ_n was calculated as described in Refs. [52,53].

In the case of ^{109}Mo and ^{110}Mo—where contributions from the daughter nuclei to the total number of β-delayed neutrons was significant—the systematic error was governed by uncertainties in the value of C in Eq. (4). The latter was derived from the error propagation of all the variables in Eq. (3), P_{nn} being the main contribution. Relative uncertainties of about 46% and 35% were obtained for ^{109}Mo and ^{110}Mo, respectively.

The P_n values and their errors obtained in the present experiment are listed in Table II and systematically presented for each isotopic chain in Fig. 9. P_n values were deduced only for nuclei with a statistically significant number of detected neutrons, i.e., with a number of detected neutrons above the number of background neutrons plus uncertainties within a 1-σ confidence level. Otherwise, only upper limits of P_n were deduced using the method described in Ref. [84]—for a Poisson distribution of detected neutrons—with the extension proposed by Hebbeker to include systematic uncertainties in the input quantities [85] (see vertical lines in Fig. 9). The upper limits were calculated for a confidence level of 68%.

IV. RESULTS AND DISCUSSION

The newly measured β-decay half-lives included in Table I and Fig. 6 (as full circles) follow a systematic decreasing trend with neutron richness, agreeing, for most of the cases, with previous measured values (empty circles).

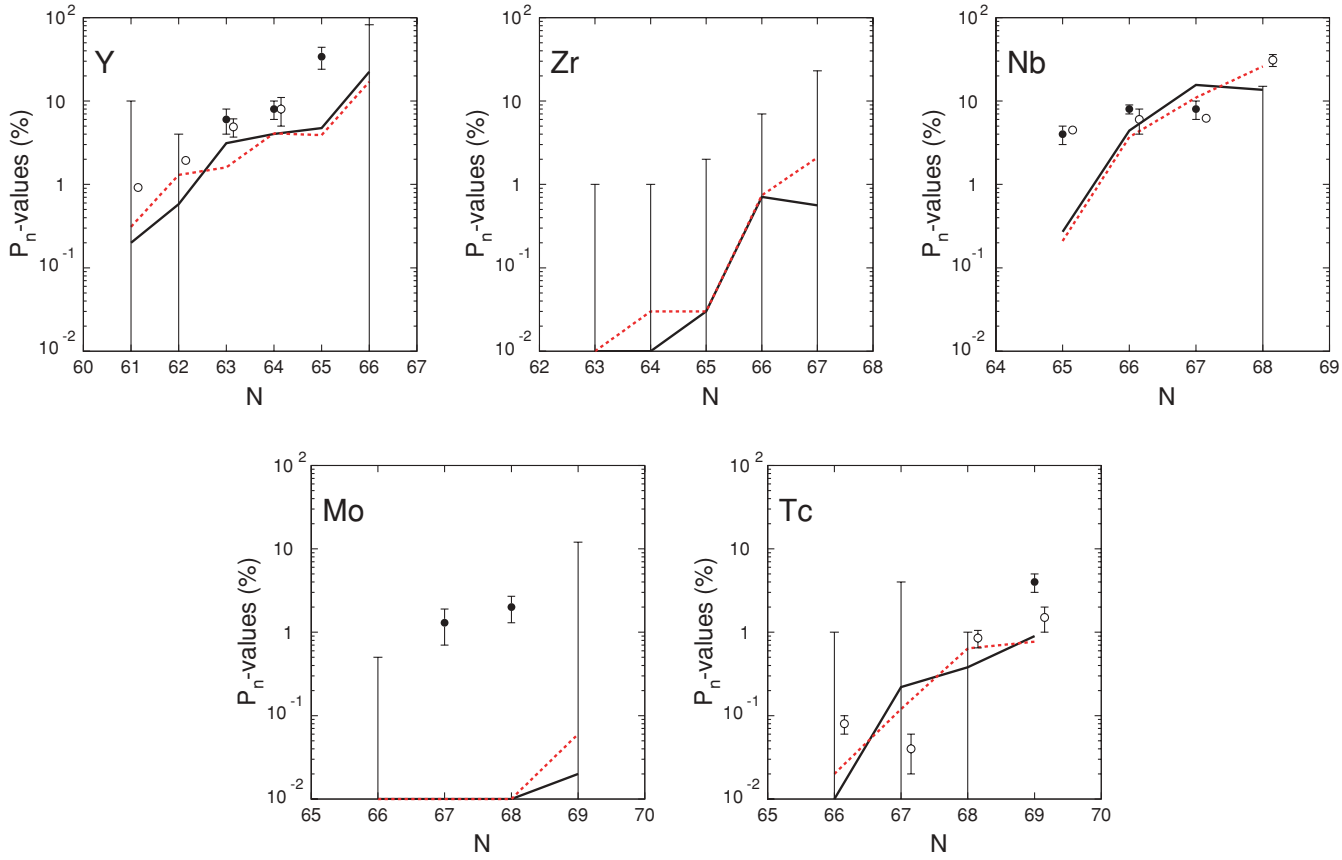

FIG. 9. (Color online) Measured P_n values (full circles) and established upper limits (segments) for Y, Zr, Nb, Mo, and Tc isotopes compared with results from previous experiments [32,33,61] (empty circles). For the sake of clarity, the latter were shifted to the right by 0.15 units. The data are compared with two versions of the QRPA model of Möller *et al.*: the version described in Ref. [41] (solid line) and the interim version QRPA06 described in Sec. IV A (dashed line) (see text for details).

In some particular cases, half-lives from β-decay isomers were found in the literature. In particular, Khan *et al.* [59] reported two different half-lives for $^{100}Y_{61}$, presumably from low- and high-spin β-decaying isomers. The $T_{1/2}$ measured in the present experiment for this nucleus is compared in Fig. 6 with the value found by Wohn *et al.* [60], presently assumed to correspond to the ground state [61]. Similarly, in the case of $^{102}Y_{63}$, two half-lives were separately reported for the low-spin [62] and high-spin [63] isomers. Interestingly enough, only the latter case is compatible with the value measured in the present experiment, thus indicating a favored production of this nucleus in a high-spin configuration.

Our results include new half-lives for the $N = 66$ midshell isotopes $^{105}Y_{66}$ and $^{106}Zr_{66}$, as well as the more exotic $^{107}Zr_{67}$ and $^{111}Mo_{69}$. New P_n values were also deduced for $^{104}Y_{65}$ and $^{109,110}Mo_{67,68}$ and new upper limits for $^{105}Y_{66}$, $^{103-107}Zr_{63-67}$ and $^{108,111}Mo_{66,69}$. In the case of $^{104}Y_{65}$, the evolution of P_n with neutron number shows a pronounced increase compared with the smooth trend observed for lighter isotopes. Conversely, the sharp increase of P_n observed by Mehren and Collaborators [32] from $P_n = (6.2 \pm 0.5)\%$, for $^{108}Nb_{67}$, to $P_n = (31 \pm 5)\%$, for $^{109}Nb_{68}$, is not supported by our measured upper limit $P_n \leqslant 15\%$ for $^{109}Nb_{68}$.

The small P_n values for $^{109,110}Mo_{67,68}$, which could not be observed in previous experiments, were detected here as a result of a lower neutron background rate of 0.001 s^{-1}. Additionally, the selectivity achieved in the present experiment, resulting from the combined in-flight separation technique and the event-by-event implantation-decay-neutron correlations made it possible to rule out any potential neutron contaminant from neutron emitters in the cocktail beam. On the contrary, Wang *et al.* [33] pointed out the possible presence of neutron-emitting contaminants from neighboring isobars in IGISOL-type experiments, which can be detected only by continuous monitoring of γ lines from the separated beam. These authors use that argument as a possible explanation for the weak components of long-lived contaminants in the $A = 104$ time-spectrum measured by Mehren *et al.* [32].

A. QRPA results

The experimental data shown in Fig. 6, for $T_{1/2}$, and in Fig. 9, for P_n, are compared to two theoretical calculations. The solid lines are the results taken from Ref. [41] (QRPA03), in which the allowed Gamow-Teller transition rates are calculated in a microscopic QRPA approach and in which the first-forbidden transition rates are obtained from the statistical gross theory [86,87]. The second calculation (henceforth referred to as QRPA06), represented by the dashed lines, gives

results from an identical model, but with the theoretical Q_β values that enter in the phase-space integrals obtained from the improved finite-range liquid-drop model (FRLDM) of Ref. [43] (corresponding to the last line in Table I of Ref. [43]). In this interim global mass model, triaxial deformation of the nuclear ground state is taken into account, but there are also some other improvements. The agreement with the 2003 mass evaluation is 0.6038 MeV. As noted elsewhere [44], there are substantial effects from axial asymmetry on the ground-state masses in precisely the region of nuclei studied in this work. When experimental masses are available for both parent and daughter Q_β and S_n are calculated from experimental data, otherwise from theory. In QRPA03, the 1995 mass evaluation from Ref. [88] was used, in the QRPA06 interim calculation, the 2003 evaluation [89] was used. Finally, both models calculate S_β assuming the same deformation for the mother and daughter nuclei, an approximation that was discussed in detail by Krumlinde and Möller for some selected cases [38]. For complete details about the model see Refs. [38–41]. Examples of how different types of nuclear structure effects manifest themselves in the calculated $T_{1/2}$ and P_n are discussed in detail in, for example, Refs. [30–37]).

1. General trends

As shown in Figs. 6 and 9, QRPA06 shows generally better agreement with the measured $T_{1/2}$ and P_n than the older QRPA03. The generally poor results for the half-lives of the less exotic isotopes are consistent with the fact that uncertainties in parameters such as Q_β have a very strong impact for decays with small energy releases. This general behavior was already observed and discussed by Pfeiffer *et al.* for different nuclei (see Figs. 8 and 9 and Tables V and VI of Ref. [27]). Beyond these general observations, the level of agreement between measured data and calculations shows no clear general systematic behavior. For instance, the half-lives predicted by both models are too short for all Y isotopes and too long for all Mo isotopes. A similar trend is seen within the same isotopic chain such as Mo, where the half-life of ^{108}Mo$_{66}$ is well reproduced, while the more exotic ^{109}Mo$_{67}$, ^{110}Mo$_{68}$, and ^{111}Mo$_{69}$ are significantly overestimated. Such "fluctuating" behavior stems from the wide variety of nuclear shapes in this shape-transition region, that are not properly described in the models.

Both QRPA03 and QRPA06 predict half-lives for all $N = 65$ isotones that are too short relative to the observed data, as was already pointed out by Wang *et al.* in their analysis of ^{104}Y$_{65}$ [33]. According to these authors, the coupling of the proton orbital $\pi[422]5/2^+$ to the neutron valence orbital $\nu[413]5/2^+$—which is in near proximity to $\nu[532]5/2^-$ at quadrupole deformation $\epsilon_2 \simeq 0.3$—would give rise to the allowed β-decay transition from ^{104}Y$_{65}0^+$ into the ^{104}Zr$_{64}0^+$ ground state with a very short half-life. This interpretation explains also the disagreement between our measured and calculated P_n for $N = 65$ isotones. In this case, the too-low P_n values predicted by QRPA reflect an overestimated β decay feeding into levels below the neutron separation energy S_n.

2. Analysis of nuclear deformations

In the case of β decay of the Y isotopes, both models behave similarly, showing too short half-lives and too low P_n values. The improved treatment of deformation in QRPA06 had no major impact when compared with QRPA03, as triaxiality is not expected to develop for these nuclei. Indeed, spectroscopic studies of Zr isotopes between $N = 60$ and $N = 64$ showed that these nuclei are dominated by increasing prolate deformations with no indication of triaxial components [90–93]. In an attempt to extend the analysis of nuclear shapes beyond ^{104}Zr$_{64}$, we have recalculated the $T_{1/2}$ and P_n of ^{104}Y$_{65}$ and ^{105}Y$_{66}$, assuming different pure prolate shapes for the corresponding mother-daughter systems. Results from this analysis are shown in Fig. 10, where the measured $T_{1/2}$ and P_n are compared with calculations performed over a large range of quadrupole deformation ($-0.35 \leqslant \epsilon_2 \leqslant 0.35$) of the daughter nuclei.

Three remarks from this analysis, in regard to the β decay of ^{104}Y$_{65}$ into ^{104}Zr$_{64}$. First, the calculated values of $T_{1/2}$ and P_n experience an abrupt transition from their maxima, for a spherical daughter ^{104}Zr$_{64}$ to very low values at deformations around $\epsilon_2 \simeq 0.1$. Second, experimental $T_{1/2}$ and P_n are reproduced assuming a prolate deformation $\epsilon_2 \sim 0.20$. Third, for larger deformations beyond $\epsilon_2 \gtrsim 0.25$ the β decay becomes faster with decreasing probabilities for β-delayed neutron emissions. The good agreement of the calculations at $\epsilon_2 \sim 0.20$ is ruled by GT transitions into four-quasiparticle levels at energies around S_n. Conversely, the too-low predicted $T_{1/2}$ and P_n are governed by the fragmentation of S_β into low-energy (i.e., well below S_n) two-quasiparticle states involving the coupling of $\pi g_{9/2}$ levels with $\nu s_{1/2}$ (at $\epsilon_2 \simeq 0.1$) or with high-$\Omega \nu d_{5/2}$ Nilsson orbitals (at $\epsilon_2 \gtrsim 0.25$). Finally, the high P_n values around 100% for β decay into a spherical ^{104}Zr$_{64}$ arises from one single GT transition to the $\pi g_{9/2} \otimes \nu g_{7/2}$ level at 7.25 MeV, well above S_n.

Similarly to ^{104}Y$_{65}$, the β-decay half-life of ^{105}Y$_{66}$ can only be correctly reproduced for deformations of the daughter ^{105}Zr$_{65}$ given by $\epsilon_2 \simeq 0.2$, whereas the P_n upper limit serves only to rule out spherical deformations. At $\epsilon_2 \simeq 0.2$, the calculated $T_{1/2}$ is governed by transitions into prolate three-quasiparticle $\pi g_{9/2} \otimes \nu d_{5/2}$ states at energies around S_n. Conversely, at larger and smaller deformations, the calculated β decay is too fast due to the presence of different low-lying one-quasiparticle states that push S_β down in energy, well below S_n. Although the measured $T_{1/2}$ is also compatible with oblate deformations $\epsilon_2 \lesssim -0.3$, we ruled out such a scenario as there is no experimental evidence of oblate shapes in lighter Zr isotopes [90–93].

In summary, the measured $T_{1/2}$ and P_n of ^{104}Y$_{65}$ and ^{105}Y$_{66}$ can be correctly reproduced only if one assumes $\epsilon_2 \sim 0.2$ for the corresponding daughter ^{104}Zr$_{64}$ and ^{105}Zr$_{65}$. On the basis of the larger elongations found for lighter Zr isotopes [90–92], the new values of ϵ_2 for ^{104}Zr and ^{105}Zr$_{65}$ contradict somehow the rather expected maximum saturated deformations at the $N = 66$ midshell. Interestingly enough, the maximum allowed quadrupole deformation of ^{104}Zr$_{64}$ deduced from our data ($\epsilon_2 \simeq 0.25$) disagrees with the large $\beta_2 \simeq 0.4$ value obtained from analysis of the quadrupole moment Q_0 of the yrast

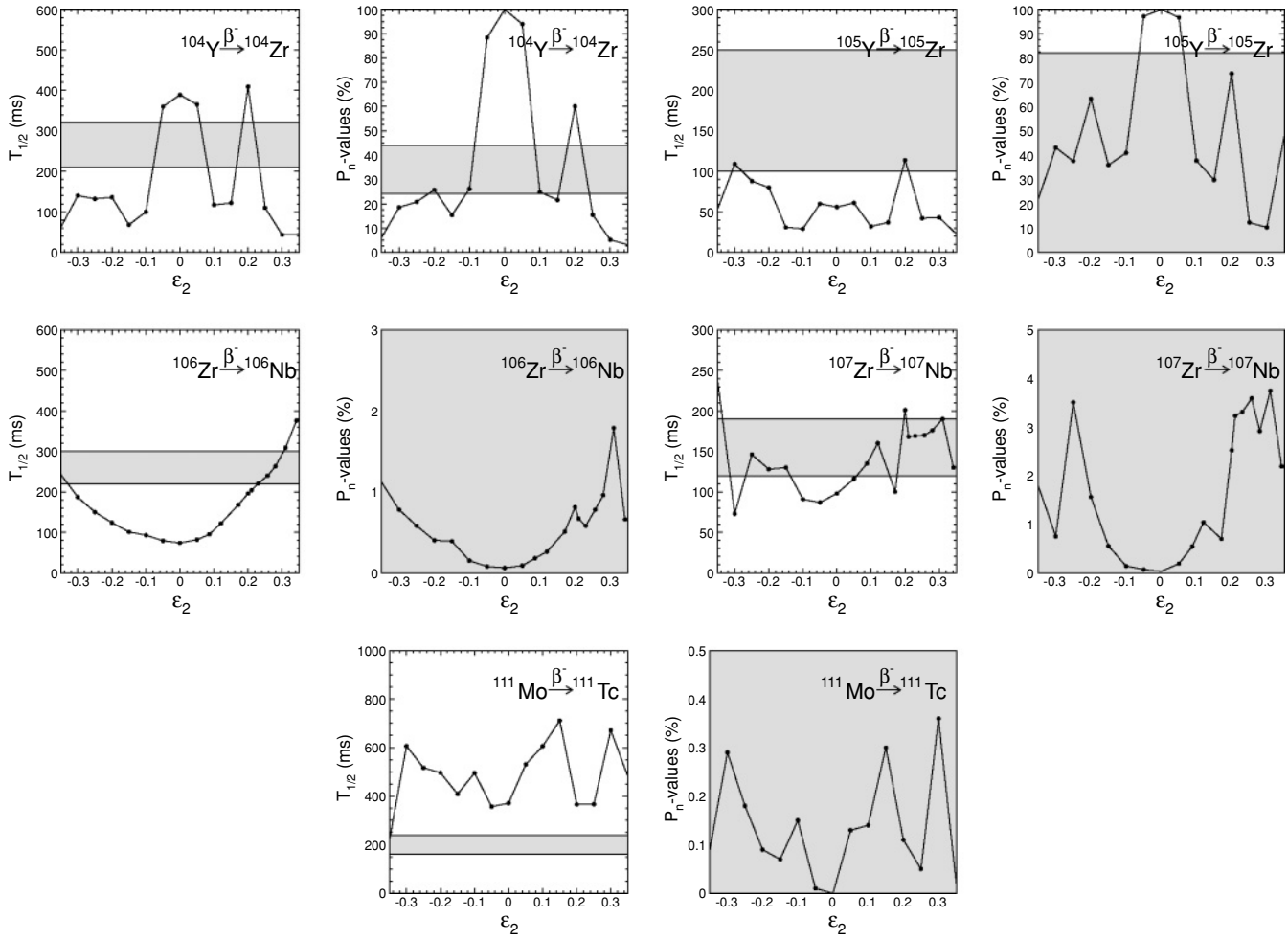

FIG. 10. QRPA-calculated β-decay half-lives and P_n values as a function of the quadrupole deformation of the daughter nuclei ϵ_2 (solid line) compared with measured data within 1-σ uncertainty (shaded area).

band [90] and from measurements of $B(E2; 2_1^+ \rightarrow 0_1^+)$ [94]. Because S_β is sensitive to the nuclear structure of the daughter nucleus—including, in addition to the yrast band, any other level from its ground state to energies just below Q_β—our result points to the possible presence of spherical or weakly deformed low-lying bands coexisting with a highly deformed yrast band of $^{104}Zr_{64}$. Spectroscopic studies of $^{100}Zr_{60}$ by Mach *et al.* [95] revealed such coexisting bands with $\beta_2 \sim 0.4$ and $\beta_2 \sim 0.2$. In addition, analysis of the Q_0 and $B(E2)$ systematics for Zr isotopes from $N = 50$ to $N = 64$ by Urban *et al.* [91] showed that coexisting spherical or weakly deformed structures may be present beyond $^{100}Zr_{60}$, although these authors claim that such phenomenon may end at $N = 64$. Because the QRPA formalism used in our analysis does not include deformation of excited levels, the $\epsilon_2 \sim 0.2$ presented here should be considered as an "effective" ground-state deformation resulting from the mixture of weakly and highly deformed bands in the daughter nuclei. Such a result suggests that shape coexistence may still be present at $^{104}Zr_{64}$ and $^{105}Zr_{65}$. This in turn may reflect the "tailing effect" of the predicted reoccurrence of the $Z = 40$ subshell, together with a new subshell $N = 70$ very far from stability [24–26] or the development of a more exotic tetrahedral shape at $^{110}Zr_{70}$ [29].

The calculated $T_{1/2}$ and P_n for $^{106}Zr_{66}$, $^{107}Zr_{67}$, and $^{111}Mo_{69}$ as a function of ϵ_2 for the corresponding mother-daughter systems are shown in Fig. 10. Here again, comparisons between the measured $T_{1/2}$ with calculations assuming pure quadrupole deformation allow constraint of the possible ϵ_2 values of $^{106}Nb_{65}$ and $^{107}Nb_{66}$, whereas the calculated P_n values do not show enough variation to distinguish between different deformations within uncertainties. The calculated $T_{1/2}$ for $^{111}Mo_{68}$ disagrees with the data for any pure quadrupole deformation of $^{111}Tc_{68}$. In this context, the FRLDM model predicts a triaxial component $\gamma = 15^\circ$ for $^{106}Nb_{65}$, $^{107}Nb_{66}$, and $^{111}Tc_{68}$, which agrees with the values deduced by Luo *et al.* for $^{105}Nb_{64}(\gamma = 13^\circ$ [96]) and $^{111}Tc_{68}(\gamma = 26^\circ$ [97]). Interestingly, the measured $T_{1/2}$ and P_n of $^{106}Zr_{66}$ and $^{107}Zr_{67}$ are in excellent agreement with the results from QRPA06 (which includes triaxiality), as shown in Fig. 6. Similarly, the calculated $T_{1/2}$ of $^{111}Mo_{69}$ is significantly improved when triaxiality is included, although no agreement with the measured value was yet found.

In summary, analysis of the new measured data for $^{106}Zr_{66}$, $^{107}Zr_{67}$, and $^{111}Mo_{69}$ using our QRPA06 calculations indicates triaxial deformations for the corresponding daughter nuclei $^{106}Nb_{65}$, $^{107}Nb_{66}$, and $^{111}Tc_{68}$.

V. SUMMARY

We have reported on the measurements of β-decay properties of neutron-rich Y, Zr, Nb, Mo, and Tc, which include new half-lives for ^{105}Y, ^{106,107}Zr, and ^{111}Mo, along with new P_n values for ^{104}Y and ^{109,110}Mo and P_n upper limits for $^{103-107}$Zr and ^{108,111}Mo. The new data could be attained due to the low β-decay background and β-delayed neutron background rates obtained with the BCS/NERO detection setup. The high selectivity of the A1900 in-flight separator at NSCL was also an instrumental achievement for the unambiguous identification of the exotic nuclei, thus demonstrating the optimum capabilities of this experiment setup to reach very exotic regions, near (and at) the r-process path.

The half-lives were analyzed using the MLH method and, in cases with enough statistics, least-squares fits of the decay curves. Agreement between both analysis brings confidence to the results. Analysis of the measured $T_{1/2}$ and P_n based on QRPA model calculations brings new insights to explore this interesting region in terms of deformations. The measured $T_{1/2}$ and P_n of $^{104,105}Y_{65,66}$ isotopes could be reproduced only for quadrupole deformation parameters ϵ_2 of the corresponding daughter nuclei $^{104,105}Zr_{64,65}$ below the values reported in the literature for $^{104}Zr_{64}$ and lighter isotopes. Because the β-strength function S_β governing the β decay from $^{104}Y_{65}$ and $^{105}Y_{66}$ is sensitive to the level structure of the corresponding daughter nuclei, we believe that the low ϵ_2 derived in the present work for $^{104}Zr_{64}$ and $^{105}Zr_{65}$ is a probable signature of coexisting weakly deformed bands. Such an interpretation is supported by previous independent analysis of deformations based on measurements of yrast-band quadrupole moments Q_0 and $B(E2)$ for Zr isotopes between $N = 50$ and $N = 64$. The deformations reported in the present article, however, show that weakly deformed bands may still be present for $^{104,105}Zr_{64,65}$. The persistence of shape coexistence for $^{104}Zr_{64}$ and $^{105}Zr_{65}$ may indicate the existence of a (near-)spherical doubly magic $^{110}Zr_{70}$ nucleus, a result that is compatible with the quenching of the $N = 82$ shell gap necessary to correct the unrealistic $A \simeq 110$ r-process abundance trough predicted by r-process model calculations.

The QRPA calculations also show that triaxial shapes play a critical role in the β decay to $^{106,107}Nb_{65,66}$ and $^{111}Tc_{68}$. The inclusion of this new deformation degree of freedom—on the basis of the new FRLDM of Möller *et al.*—significantly improves the calculated $T_{1/2}$ and P_n with respect to the new measured values. In addition, the FRLDM-predicted triaxial components are compatible with values reported in the literature for nuclei in this region.

Extension of β decay and spectroscopic experimental studies to full r-process nuclei requires new high-intensity fragmentation-beam facilities like FRIB at NSCL, FAIR at GSI, and RIBF at RIKEN. These measurements are necessary to understand the nuclear physics governing the r process. New measurements of masses and Q_β values of $N = 82$ r-process isotones below Sn will clarify the role of shell quenching in the synthesis of heavy nuclei.

ACKNOWLEDGMENTS

The authors thank the NSCL operations staff for providing the primary beam, as well as T. Ginter and the A1900 staff for the planning and development of the fragments analyzed in the present article. Fruitful discussions with R. Fox during the preparation of the experiment are acknowledged. The authors are also grateful to T. Hebbeker for letting them use his method and code to calculate upper limits. This work was supported in part by the Joint Institute for Nuclear Astrophysics (JINA) under NSF Grant PHY-02-16783 and the National Superconducting Cyclotron Laboratory (NSCL) under NSF Grant PHY-01-10253.

APPENDIX: MAXIMUM LIKELIHOOD ANALYSIS OF HALF-LIVES

The maximum likelihood method is the mathematical correct description even in cases of poor statistics. Let a set of independently measured quantities x_i originate from a probability density function $f(x_i, \boldsymbol{\alpha})$, where $\boldsymbol{\alpha}$ is a set of unknown parameters. The maximum likelihood method consists of finding a parameter set $\boldsymbol{\alpha}$ that maximizes the joint probability density

$$\mathcal{L}(\boldsymbol{\alpha}) = \prod_i f(x_i, \boldsymbol{\alpha}),$$

for all measured data points x_i. $\mathcal{L}$ is also called the likelihood function. In most cases, it is easier to use $\ln \mathcal{L}$ instead and to solve the likelihood equation

$$\frac{\partial \ln \mathcal{L}}{\partial \boldsymbol{\alpha}} = 0.$$

Normalization factors, which depend on the set of parameters $\boldsymbol{\alpha}$ have to be included in the maximization process. All other multiplicative constants in the $f(x_i, \boldsymbol{\alpha})$ can be neglected, even if they depend on the measured quantities x_i.

The individual decay events of a decay sequence are not statistically independent, therefore the likelihood function has to be defined. Additional corrections must be used to compensate for the neglected late decay events, if the correlation time window is small compared to the mean lifetime of the investigated nuclei. A method only using the first measured decay event within the correlation window is reported in Ref. [73]. Such a method does not make use of all available information and therefore might be disadvantageous in the case of poor statistics. Based on the work in Ref. [98], the mathematical correct probability density function for up to three decay events within the correlation time window was developed.

We assumed that all the decay events after an implantation of an identified nucleus within a position and time correlation interval belong to the first three decay generation (mother, daughter, and granddaughter decay). Additionally, coincidentally assigned background events with a constant rate might

occur. Up to three events within the time correlation window are considered. For the sake of simplicity, we will exclude in the present discussion the β-delayed neutron branchings.

Let λ_1, λ_2, and λ_3 be the decay constants for the decay of a mother, daughter, and granddaughter nucleus, respectively. It is important to distinguish the probability for a decay within a time t characterized by a decay constant λ_1

$$F_1(\lambda_1, t) = 1 - e^{-\lambda_1 t},$$

from the probability density function for a decay at exact time t characterized by a decay constant λ_1

$$f_1(\lambda_1, t) = \lambda_1 e^{-\lambda_1 t}.$$

For the detection of the second decay generation, we use the probability for a decay within a time t of a daughter nuclei with a decay constant λ_2, which was populated by a mother decay with decay constant λ_1:

$$F_2(\lambda_1, \lambda_2, t) = 1 - \frac{\lambda_1\lambda_2}{\lambda_2 - \lambda_1}\left(\frac{e^{-\lambda_1 t}}{\lambda_1} - \frac{e^{-\lambda_2 t}}{\lambda_2}\right),$$

and the probability density function for a decay of a daughter nuclei with a decay constant λ_2 at time t, which was populated by a mother decay with decay constant λ_1:

$$f_2(\lambda_1, \lambda_2, t) = \frac{\lambda_1\lambda_2}{\lambda_2 - \lambda_1}(e^{-\lambda_1 t} - e^{-\lambda_2 t}).$$

Similarly, the probability F_3, and the corresponding probability density function f_3, for a decay within a time t of a granddaughter nuclei with a decay constant λ_3, which was populated by a mother and daughter decay characterized by decay constants λ_1 and λ_2 are given by:

$$\begin{aligned} &F_3(\lambda_1, \lambda_2, \lambda_3, t) \\ &\quad = 1 - \frac{\lambda_1\lambda_2\lambda_3}{(\lambda_2 - \lambda_1)(\lambda_3 - \lambda_1)(\lambda_3 - \lambda_2)} \\ &\qquad \times \left(\frac{\lambda_3 - \lambda_2}{\lambda_1}e^{-\lambda_1 t} - \frac{\lambda_3 - \lambda_1}{\lambda_2}e^{-\lambda_2 t} + \frac{\lambda_2 - \lambda_1}{\lambda_3}e^{-\lambda_3 t}\right), \end{aligned}$$

and

$$\begin{aligned} &f_3(\lambda_1, \lambda_2, \lambda_3, t) \\ &\quad = \frac{\lambda_1\lambda_2\lambda_3}{(\lambda_2 - \lambda_1)(\lambda_3 - \lambda_1)(\lambda_3 - \lambda_2)}[(\lambda_3 - \lambda_2)e^{-\lambda_1 t} \\ &\qquad - (\lambda_3 - \lambda_1)e^{-\lambda_2 t} + (\lambda_2 - \lambda_1)e^{-\lambda_3 t}]. \end{aligned}$$

Finally, for background events, the average rate and the expected number of events within the correlation time is known. The probability for the observation of exact r background events within a correlation time t_c and a background rate b can be calculated using Poisson statistics:

$$B_r = \frac{(bt_c)^r e^{-bt_c}}{r!}.$$

Depending on the number of observed decay events within the correlation time, one has to consider all possible scenarios leading to the observation. In the following, we use a short notation to identify the composition of the probability terms of the various scenarios. D_i stands for the probability that a decay of the i-th generation occurs and O_i that an occurring decay is observed. ϵ_1, ϵ_2, and ϵ_3 designate the detection efficiencies for the respective decays, i.e., the probability for the observation of an ocurring decay. In addition, the notations $\bar{F}(\lambda, t) = 1 - F(\lambda, t)$ and $\bar{\epsilon} = 1 - \epsilon$ are used.

The probability for the observation of no decay event within the correlation time can be calculated as follows:

$$\begin{aligned} P_0(\lambda_1) &= (\bar{D}_1 + D_1\bar{O}_1\bar{D}_2 + D_1\bar{O}_1D_2\bar{O}_2\bar{D}_3 \\ &\quad + D_1\bar{O}_1D_2\bar{O}_2D_3\bar{O}_3)B_0 \\ P_0(\lambda_1) &= \{\bar{F}_1(\lambda_1, t_c) + [\bar{F}_2(\lambda_1, \lambda_2, t_c) - \bar{F}_1(\lambda_1, t_c)]\bar{\epsilon}_1 \\ &\quad + [\bar{F}_3(\lambda_1, \lambda_2, \lambda_3, t_c) - \bar{F}_2(\lambda_1, \lambda_2, t_c)]\bar{\epsilon}_1\bar{\epsilon}_2 \\ &\quad + F_3(\lambda_1, \lambda_2, \lambda_3, t_c)\bar{\epsilon}_1\bar{\epsilon}_2\bar{\epsilon}_3\}B_0 \\ &= [1 - F_1(\lambda_1, t_c)\epsilon_1 - F_2(\lambda_1, \lambda_2, t_c)\bar{\epsilon}_1\epsilon_2 \\ &\quad - F_3(\lambda_1, \lambda_2, \lambda_3, t_c)\bar{\epsilon}_1\bar{\epsilon}_2\epsilon_3]B_0. \end{aligned}$$

For the case of the observation of only one decay event within the correlation time, four scenarios are possible:

(i) The decay of the mother was observed, daughter and granddaughter decay did either not occur or these decays were not observed:

$$P_{101} = P(d_1) = D_1O_1(\bar{D}_2 + D_2\bar{O}_2\bar{D}_3 + D_2\bar{O}_2D_3\bar{O}_3)B_0.$$

(ii) The decay of mother and daughter did occur, but only the daughter decay was observed, whereas the granddaughter decay did not occur or was not observed:

$$P_{102} = P(d_2) = D_1\bar{O}_1D_2O_2(\bar{D}_3 + D_3\bar{O}_3)B_0.$$

(iii) All three decays did occur, but only the granddaughter decay was observed:

$$P_{103} = P(d_3) = D_1\bar{O}_1D_2\bar{O}_2D_3O_3B_0.$$

Until now, we assumed that there was no background event within the correlation time.

(iv) The last scenario describes the observation of a background event, all three decays did not occur or were not observed:

$$\begin{aligned} P_{104} = P(b) &= (\bar{D}_1 + D_1\bar{O}_1\bar{D}_2 + D_1\bar{O}_1D_2\bar{O}_2\bar{D}_3 \\ &\quad + D_1\bar{O}_1D_2\bar{O}_2D_3\bar{O}_3)B_1. \end{aligned}$$

Calculation of the likelihood function requires the probability density functions for the observations of a single decay event at time t_1:

$$\begin{aligned} p_{101}(\lambda_1) &= C_1 f_1(\lambda_1, t_1)\epsilon_1\{\bar{F}_1(\lambda_2, t_c - t_1) \\ &\quad + [\bar{F}_2(\lambda_2, \lambda_3, t_c - t_1) - \bar{F}_1(\lambda_2, t_c - t_1)]\bar{\epsilon}_2 \\ &\quad + F_2(\lambda_2, \lambda_3, t_c - t_1)\bar{\epsilon}_2\bar{\epsilon}_3\}B_0 \\ &= C_1 f_1(\lambda_1, t_1)\epsilon_1[1 - F_1(\lambda_2, t_c - t_1)\epsilon_2 \\ &\quad - F_2(\lambda_2, \lambda_3, t_c - t_1)\bar{\epsilon}_2\epsilon_3]B_0, \\ p_{102}(\lambda_1) &= C_1 f_2(\lambda_1, \lambda_2, t_1)\bar{\epsilon}_1\epsilon_2[\bar{F}_1(\lambda_3, t_c - t_1) \\ &\quad + F_1(\lambda_3, t_c - t_1)\bar{\epsilon}_3]B_0 \\ &= C_1 f_2(\lambda_1, \lambda_2, t_1)\bar{\epsilon}_1\epsilon_2[1 - F_1(\lambda_3, t_c - t_1)\epsilon_3]B_0, \\ p_{103}(\lambda_1) &= C_1 f_3(\lambda_1, \lambda_2, \lambda_3, t_1)\bar{\epsilon}_1\bar{\epsilon}_2\epsilon_3 B_0, \end{aligned}$$

$$
\begin{aligned}
p_{104}(\lambda_1) &= C_1\{\bar{F}_1(\lambda_1, t_c) + [\bar{F}_2(\lambda_1, \lambda_2, t_c) - \bar{F}_1(\lambda_1, t_c)]\bar{\epsilon}_1 \\
&\quad + [\bar{F}_3(\lambda_1, \lambda_2, \lambda_3, t_c) - \bar{F}_2(\lambda_1, \lambda_2, t_c)]\bar{\epsilon}_1\bar{\epsilon}_2 \\
&\quad + F_3(\lambda_1, \lambda_2, \lambda_3, t_c)\bar{\epsilon}_1\bar{\epsilon}_2\bar{\epsilon}_3\}B_1 t_c^{-1} \\
&= C_1[1 - F_1(\lambda_1, t_c)\epsilon_1 - F_2(\lambda_1, \lambda_2, t_c)\bar{\epsilon}_1\epsilon_2 \\
&\quad - F_3(\lambda_1, \lambda_2, \lambda_3, t_c)\bar{\epsilon}_1\bar{\epsilon}_2\epsilon_3]B_1 t_c^{-1}.
\end{aligned}
$$

The joint probability density function for observing one decay event at time t_1 is the sum of the single probability densities:

$$p_1(\lambda_1) = p_{101}(\lambda_1) + p_{102}(\lambda_1) + p_{103}(\lambda_1) + p_{104}(\lambda_1),$$

where the normalization constant C_1 fulfills the equation:

$$\int_0^{t_c} p_1(\lambda_1)\, dt_1 = 1.$$

Ten different scenarios need to be considered when two decay events occur within t_c, and 20 different scenarios for three decay events. A detailed description of all scenarios and the resulting normalized joint probability functions $p_2(\lambda_1)$ and $p_3(\lambda_1)$ can be found in Refs. [98,99].

The analysis program assigns decay events to preceding implantations, only events with one ($n_i = 1$), two ($n_i = 2$), or three ($n_i = 3$) decay events within the correlation time are considered. Therefore, we initially maximize the likelihood function for N_{123} observed decay sequences:

$$
\begin{aligned}
\mathcal{L}_{123}(\lambda_1) = \prod_{i=1}^{N_{123}} &[\delta(n_i - 1)p_1(\lambda_1) + \delta(n_i - 2)p_2(\lambda_1) \\
&+ \delta(n_i - 3)p_3(\lambda_1)].
\end{aligned}
$$

The solution $\hat{\lambda}_{1_0}$ of the maximization equation

$$\frac{\partial \mathcal{L}_{123}(\lambda_1)}{\partial \lambda_1} = 0$$

has to be corrected for events with no observed decay events within the correlation time window. The most likely number of events N_0 of this type depends on $P_0(\lambda_1)$ and therefore on λ_1 itself:

$$N_0 = \frac{P_0(\lambda_1)}{1 - P_0(\lambda_1)} N_{123}.$$

To find the solution $\hat{\lambda}_{1_{j+1}}$ of the maximization equation of the joint likelihood function $\mathcal{L}$, an iterative numerical method is used until $\hat{\lambda}_1$ converges:

$$\mathcal{L}_{(j+1)}(\lambda_1) = \mathcal{L}_{123}(\lambda_1) P_0(\lambda_1)^{N_0(\hat{\lambda}_{1_j})},$$

$$\left.\frac{\partial \mathcal{L}_{(j+1)}(\lambda_1)}{\partial \lambda_1}\right|_{\lambda_1 = \hat{\lambda}_{1_{(j+1)}}} = 0.$$

The correlation time, therefore, should be long compared to the mean life time of the mother nuclei to avoid large correction factors due to this iterative method. If the background rate is low enough, a correlation time equal to 10 half-lives should be used. If the time window is too long, the assumption of a maximum number of three decays within the correlation time is no longer valid and the maximum likelihood method might fail.

The validity of this approximation as well as a check of the whole procedure for the analysis of decay sequences was thoroughly discussed in Ref. [99].

[1] E. M. Burbidge, G. R. Burbidge, W. A. Fowler, and F. Hoyle, Rev. Mod. Phys. **29**, 547 (1957).
[2] A. G. W. Cameron, Publ. Astron. Soc. Pac. **69**, 201 (1957).
[3] J. J. Cowan, F.-K. Thielemann, and J. W. Truran, Phys. Rep. **208**, 267 (1991).
[4] J. W. Truran, J. J. Cowan, C. A. Pilachowski, and C. Sneden, Publ. Astron. Soc. Pac. **114**, 1293 (2002).
[5] J. J. Cowan, C. Sneden, J. E. Lawler, and E. A. Den Hartog, in *Proceedings of Science*, PoS (NIC-IX), 014 (2006); http://pos.sissa.it//archive/conferences/028/014/NIC-IX_014.pdf.
[6] J. A. Johnson, Astrophys. J. Suppl. Ser. **139**, 219 (2002).
[7] C. Sneden, J. J. Cowan, J. E. Lawer, I. I. Ivans, S. Burles, T. C. Beers, F. Primas, V. Hill, J. W. Truran, G. M. Fuller, B. Pfeiffer, and K.-L. Kratz, Astrophys. J. **591**, 936 (2003).
[8] W. Aoki, S. Honda, T. C. Beers, and C. Sneden, Astrophys. J. **586**, 506 (2003).
[9] P. S. Barklem, N. Christlieb, T. C. Beers, V. Hill, M. S. Bessell, J. Holmberg, B. Marsteller, S. Rossi, F.-J. Zickgraf, and D. Reimers, Astron. Astrophys. **439**, 129 (2005).
[10] C. Travaglio, R. Gallino, E. Arnone, J. J. Cowan, F. Jordan, and C. Sneden, Astrophys. J. **601**, 864 (2004).
[11] F. Montes, T. C. Beers, J. J. Cowan, T. Elliot, K. Farouqi, R. Gallino, M. Heil, K.-L. Kratz, B. Pfeiffer, M. Pignatari, and H. Schatz, Astrophys. J. **671**, 1685 (2007).
[12] K. L. Kratz, K. Farouqi, B. Pfeiffer, J. W. Truran, C. Sneden, and J. J. Cowan, Astrophys. J. **662**, 39 (2007).
[13] F. Farouqi, K.-L. Kratz, J. J. Cowan, L. I. Mashonkina, B. Pfeiffer, C. Sneden, F.-K. Thielemann, and J. W. Truran, AIP Conf. Proc. **990**, 309 (2008).
[14] K. L. Kratz, F. Farouqi, L. I. Mashonkina, and B. Pfeiffer, New Astron. Rev. **52**, 390 (2008).
[15] J. H. Reynolds, Phys. Rev. Lett. **4**, 8 (1960).
[16] D.-C. Lee and A. N. Halliday, Nature (London) **378**, 771 (1995).
[17] U. Ott and K. L. Kratz, New Astron. Rev. **52**, 396 (2008).
[18] Y.-Z. Qian, W. C. Haxton, K. Langanke, and P. Vogel, Phys. Rev. C **55**, 1532 (1997).
[19] K.-L. Kratz, J.-P. Bitouzet, F.-K. Thielemann, P. Möller, and B. Pfeiffer, Astrophys. J. **403**, 216 (1993).
[20] B. Chen, J. Dobaczewski, K.-L. Kratz, K. Langanke, B. Pfeiffer, F.-K. Thielemann, and P. Vogel, Phys. Lett. **B355**, 37 (1995).
[21] J. M. Pearson, R. C. Nayak, and S. Goriely, Phys. Lett. **B387**, 455 (1996).
[22] B. Pfeiffer, K.-L. Kratz, and F.-K. Thielemann, Z. Phys. A **357**, 235 (1997).
[23] I. Dillmann, K.-L. Kratz, A. Wöhr, O. Arndt, B. A. Brown, P. Hoff, M. Hjorth-Jensen, U. Köster, A. N. Ostrowski, B. Pfeiffer, D. Seweryniak, J. Shergur, and W. B. Walters, Phys. Rev. Lett. **91**, 162503 (2003).

[24] J. Dobaczewski, I. Hamamoto, W. Nazarewicz, and J. A. Sheikh, Phys. Rev. Lett. **72**, 981 (1994).
[25] J. Dobaczewski, W. Nazarewicz, T. R. Werner, J. F. Berger, C. R. Chinn, and J. Dechargé, Phys. Rev. C **53**, 2809 (1996).
[26] B. Pfeiffer, K.-L. Kratz, J. Dobaczewski, and P. Möller, Acta Phys. Pol. B **27**, 475 (1996).
[27] B. Pfeiffer, K.-L. Kratz, F.-K. Thielemann, and W. B. Walters, Nucl. Phys. **A693**, 282 (2001).
[28] J. Dudek, A. Góźdź, N. Schunck, and M. Miśkiewicz, Phys. Rev. Lett. **88**, 252502 (2002).
[29] N. Schunck, J. Dudek, A. Góźdź, and P. H. Regan, Phys. Rev. C **69**, 061305(R) (2004).
[30] K.-L. Kratz, Nucl. Phys. **A417**, 447 (1984).
[31] O. Sorlin, D. Guillemaud-Mueller, A. C. Mueller, V. Borrel, S. Dogny, F. Pougheon, K.-L. Kratz, H. Gabelmann, B. Pfeiffer, A. Wöhr, W. Ziegert, Y. E. Penionzhkevich, S. M. Lukyanov, V. S. Salamatin, R. Anne, C. Borcea, L. K. Fifield, M. Lewitowicz, M. G. Saint-Laurent, D. Bazin, C. Détraz, F.-K. Thielemann, and W. Hillebrandt, Phys. Rev. C **47**, 2941 (1993).
[32] T. Mehren, B. Pfeiffer, S. Schoedder, K.-L. Kratz, M. Huhta, P. Dendooven, A. Honkanen, G. Lhersonneau, M. Oinonen, J.-M. Parmonen, H. Penttilä, A. Popov, V. Rubchenya, and J. Äystö, Phys. Rev. Lett. **77**, 458 (1996).
[33] J. C. Wang, P. Dendooven, M. Hannawald, A. Honkanen, M. Huhta, A. Jokinen, K.-L. Kratz, G. Lhersonneau, M. Oinonen, H. Penttilä, K. Peräjärvi, B. Pfeiffer, and J. Äystö, Phys. Lett. **B454**, 1 (1999).
[34] K.-L. Kratz, P. Möller, F.-K. Thielemann, and W. B. Walters, AIP Conf. Proc. **529**, 295 (2000).
[35] M. Hannawald, K. L. Kratz, B. Pfeiffer, W. B. Walters, V. N. Fedoseyev, V. I. Mishin, W. F. Mueller, H. Schatz, J. Van Roosbroeck, U. Köster, V. Sebastian, and H. L. Ravn (ISOLDE Collaboration), Phys. Rev. C **62**, 054301 (2000).
[36] A. Wöhr, A. Ostrowski, K.-L. Kratz, I. Dillmann, A. M. El-Taher, V. Fedoseyev, L. Fraile, H. Fynbö, U. Kösler, B. Pfeiffer, H. L. Ravn, M. Seliverstov, J. Shergur, L. Weissman, and W. B. Walters (ISOLDE Collaboration), in *Proceedings of the 11th Workshop on Nuclear Astrophysics, Ringberg Castle, Germany, 2002*, edited by W. Hillebrand and E. Müller (MPI für Astrophysik Garching, 2002), p. 79.
[37] F. Montes, A. Estrade, P. T. Hosmer, S. N. Liddick, P. F. Mantica, A. C. Morton, W. F. Mueller, M. Ouellette, E. Pellegrini, P. Santi, H. Schatz, A. Stolz, B. E. Tomlin, O. Arndt, K.-L.Kratz, B. Pfeiffer, P. Reeder, W. B. Walters, A. Aprahamian, and A. Wöhr, Phys. Rev. C **73**, 035801 (2006).
[38] J. Krumlinde and P. Möller, Nucl. Phys. **A417**, 419 (1984).
[39] P. Möller and J. Randrup, Nucl. Phys. **A514**, 1 (1990).
[40] P. Möller, J. R. Nix, and K.-L. Kratz, At. Data Nucl. Data Tables **66**, 131 (1997).
[41] P. Möller, B. Pfeiffer, and K.-L. Kratz, Phys. Rev. C **67**, 055802 (2003).
[42] P. Möller, J. R. Nix, W. D. Myers, and W. J. Swiatecki, At. Data Nucl. Data Tables **59**, 185 (1995).
[43] P. Möller, R. Bengtsson, K.-L. Kratz, and H. Sagawa, in *Proceedings of the International Conference on Nuclear Data Science and Technology*, *Nice, France, 2007*, edited by O. Bersillon, F. Gunsing, E. Bauge, R. Jacqmin, and S. Leray (EDP Sciences, 2008), p. 69.
[44] P. Möller, R. Bengtsson, B. G. Carlsson, P. Olivius, T. Ichikawa, H. Sagawa, and A. Iwamoto, At. Data Nucl. Data Tables **94**, 758 (2008).
[45] The $K500 \otimes K1200$, A Coupled Cyclotron Facility at the National Superconducting Cyclotron Laboratory, NSCL Report MSUCL-939, 1994 (unpublished).
[46] D. J. Morrissey, B. M. Sherrill, M. Steiner, A. Stolz, and I. Wiedenhoever, Nucl. Instrum. Methods Phys. Res. B **204**, 90 (2003).
[47] K.-H. Schmidt, E. Hanelt, H. Geissel, G. Münzenberg, and J.-P. Dufour, Nucl. Instrum. Methods Phys. Res. A **260**, 287 (1987).
[48] P. Sigmund, *Particle Penetration and Radiation Effects* (Springer-Verlag, Berlin/Heidelberg, 2006), Vol. 151.
[49] J. I. Prisciandaro, A. C. Morton, and P. F. Mantica, Nucl. Instrum. Methods Phys. Res. A **505**, 140 (2003).
[50] D. Bazin, O. B. Tarasov, M. Lewitowicz, and O. Sorlin, Nucl. Instrum. Methods A **482**, 307 (2002).
[51] J. F. Ziegler, J. P. Biersack, and U. Littmar, *The Stopping and Range of Ions in Solids* (Pergamon Press, New York, 1985), Vol. 1.
[52] G. Lorusso, J. Pereira, P. Hosmer, L. Kern, H. Schatz, F. Montes, P. Santi, H. Schatz, and F. Schertz, in *Proceedings of Science*, PoS (NIC-IX), 243 (2006); http://pos.sissa.it//archive/conferences/028/243/NIC-IX_243.pdf.
[53] G. Lorusso, J. Pereira *et al.* (in preparation).
[54] P. T. Hosmer, Ph.D. thesis, Michigan State University, 2005.
[55] W. F. Mueller, J. A. Church, T. Glasmacher, D. Gutknecht, G. Hackman, P. G. Hansen, Z. Hu, K. L. Miller, and P. Quirin, Nucl. Instrum. Methods Phys. Res. A **466**, 492 (2001).
[56] B. E. Tomlin, Ph.D. thesis, Michigan State University, 2006.
[57] B. E. Tomlin, P. F. Mantica, and W. B. Walters, Eur. Phys. J Spec. Top. **150**, 183 (2007).
[58] J. Cetnar, Ann. Nucl. Energy **33**, 640 (2006).
[59] T. A. Khan, W. D. Lauppe, K. Sistemich, H. Lawin, G. Sadler, and H. A. Selle, Z. Phys. A **283**, 105 (1977).
[60] F. K. Wohn, J. C. Hill, C. B. Howard, K. Sistemich, R. F. Petry, R. L. Gill, H. Mach, and A. Piotrowski, Phys. Rev. C **33**, 677 (1986).
[61] Evaluated Nuclear Structure Data File; http//www.nndc.bnl.gov/ensdf.
[62] J. C. Hill, D. D. Schwellenbach, F. K. Wohn, J. A. Winger, R. L. Gill, H. Ohm, and K. Sistemich, Phys. Rev. C **43**, 2591 (1991).
[63] K. Shizuma, J. C. Hill, H. Lawin, M. Shaanan, H. A. Selic, and K. Sistemich, Phys. Rev. C **27**, 2869 (1983).
[64] A. Schmitt, N. Kaffrell, and N. Trautmann, Inst. für Kernchemie, Univ. Mainz, Jahresbericht **1979**, 34 (1980).
[65] K. Shizuma, H. Lawin, and K. Sistemich, Z. Phys. A **311**, 71 (1983).
[66] J. Äystö, A. Astier, R. Beraud, T. Enqvist, K. Eskola, Z. Janas, P. P. Jauho, A. Jokinen, M. Leino, S. Malm, J. Parmonen, H. Penttilä, and J. Zylicz, JYFL 24 (1991).
[67] A. Jokinen, T. Enqvist, P. P. Jauho, M. Leino, J. M. Parmonen, H. Penttilä, J. Äystö, and K. Eskola, Nucl. Phys. **A584**, 489 (1995).
[68] J. Äystö, A. Astier, T. Enqvist, K. Eskola, Z. Janas, A. Jokinen, K.-L. Kratz, M. Leino, H. Penttilä, B. Pfeiffer, and J. Zylicz, Phys. Rev. Lett. **69**, 1167 (1992).
[69] J. C. Wang, P. Dendooven, A. Honkanen, M. Huikari, A. Jokinen, V. S. Kolhinen, G. Lhersonneau, A. Nieminen, K. Peräjärvi, S. Rinta-Antila, and J. Äystö, Eur. Phys. J. A **19**, 83 (2004).

[70] J. Äystö, P. P. Jauho, Z. Janas, A. Jokinen, J. Parmonen, H. Penttilä, P. Taskinen, R. Béraud, R. Duffait, A. Emsallem, J. Meyer, M. Meyer, N. Redon, M. E. Leino, K. Eskola, and P. Dendooven, Nucl. Phys. **A515**, 365 (1990).
[71] P. T. Hosmer, H. Schatz, A. Aprahamian, O. Arndt, R. R. C. Clement, A. Estrade, K.-L. Kratz, S. N. Liddick, P. F. Mantica, W. F. Mueller, F. Montes, A. C. Morton, M. Ouellette, E. Pellegrini, B. Pfeiffer, P. Reeder, P. Santi, M. Steiner, A. Stolz, B. E. Tomlin, W. B. Walters, and A. Wöhr, Phys. Rev. Lett. **94**, 112501 (2005).
[72] K.-H. Schmidt, C.-C. Sahm, K. Pielenz, and H.-G. Clerc, Z. Phys. A **316**, 19 (1984).
[73] M. Bernas, P. Armbruster, J. P. Bocquet, R. Bissot, H. Faust, Ch. Kozhuharov, and J. L. Sida, Z. Phys. A **336**, 41 (1990).
[74] R. Schneider, T. Faestermann, J. Friese, R. Gernhäuser, H. Geissel, H. Gilg, F. Heine, J. Homolka, P. Kienle, H.-J. Körner, G. Münzenberg, J. Reinhold, K. Sümmerer, and K. Zeitelhack, Nucl. Phys. **A616**, 341c (1997).
[75] K. Sümmerer, R. Schneider, T. Faestermann, J. Friese, H. Geissel, R. Gernhäuser, H. Gilg, F. Heine, J. Homolka, P. Kienle, H.-J. Körner, G. Münzenberg, J. Reinhold, and K. Zeitelhack, Nucl. Phys. **A616**, 341c (1997).
[76] A. Ianni, Nucl. Instrum. Methods Phys. Res. A **516**, 184 (2004).
[77] W. Brüchle, Radiochimica acta **91**, 71 (2003).
[78] R. Barlow, arXive:physics/0406120 (2004).
[79] Computer code MCNP 5.0 ORNL (RCICC), Oak Ridge, TN, 2003.
[80] K.-L. Kratz, in *Proceedings of the Consultants' Meeting on Delayed Neutron Properties* (IAEA, Vienna, 1979), p. 103.
[81] K.-L. Kratz, W. Rudolph, H. Ohm, H. Franz, M. Zendel, G. Hermann, S. G. Prussin, F. M. Nuh, A. A. Shihab-Eldin, D. R. Slaughter, W. Halverson, and H. V. Klapdor, Nucl. Phys. **A317**, 335 (1979).
[82] K.-L. Kratz, A. Schröder, H. Ohm, M. Zendel, H. Gabelmann, W. Ziegert, P. Peuser, G. Jung, B. Pfeiffer, K. D. Wünsch, H. Wollnik, C. Ristori, and J. Crançon, Z. Phys. A **306**, 239 (1982).
[83] T. R. England, E. D. Arthur, M. C. Brady, and R. J. LaBauve, Los Alamos National Laboratory Report LA-11151-MS, 1998.
[84] G. Cowan, *Statistical Data Analysis* (Oxford University Press, New York, 1998).
[85] T. Hebbeker (private communication); http://www-eep.phsik.hu-berlin.de/ hebbeker/plimits.html.
[86] K. Takahashi, Prog. Theor. Phys. **47**, 1500 (1972).
[87] K. Takahashi, M. Yamada, and T. Kondoh, At. Data Nucl. Data Tables **12**, 101 (1973).
[88] G. Audi and A. H. Wapstra, Nucl. Phys. **A595**, 409 (1995).
[89] G. Audi, A. H. Wapstra, and C. Thibault, Nucl. Phys. **A729**, 337 (2003).
[90] A. G. Smith, J. L. Durell, W. R. Phillips, M. A. Jones, M. Leddy, W. Urban, B. J. Varley, I. Ahmad, L. R. Morss, M. Bentaleb, A. Guessous, E. Lubkiewicz, N. Schulz, and R. Wyss, Phys. Rev. Lett. **77**, 1711 (1996).
[91] W. Urban, J. L. Durell, A. G. Smith, W. R. Phillips, M. A. Jones, B. J. Varley, T. Rząca-Urban, I. Ahmad, L. R. Morss, M. Bentaleb, and N. Schulz, Nucl. Phys. **A689**, 605 (2001).
[92] H. L. Thayer, J. Billowes, P. Campbell, P. Dendooven, K. T. Flanagan, D. H. Forest, J. A. R. Griffith, J. Huikari, A. Jokinen, R. Moore, A. Nieminen, G. Tungate, S. Zemlyanoi, and J. Äystö, J. Phys. G: Nucl. Part. Phys. **29**, 2247 (2003).
[93] H. Hua, C. Y. Wu, D. Cline, A. B. Hayes, R. Teng, R. M. Clark, P. Fallon, A. Goergen, A. O. Macchiavelli, and K. Vetter, Phys. Rev. C **69**, 014317 (2004).
[94] C. Goodin, Y. X. Luo, J. K. Hwang, A. V. Ramayya, J. H. Hamilton, J. O. Rasmussen, S. J. Zhu, A. Gelberg, and G. M. Ter-Akopian, Nucl. Phys. **A787**, 231c (2007).
[95] H. Mach, M. Moszyński, R. L. Gill, F. K. Wohn, J. A. Winger, J. C. Hill, G. Molnár, and K. Sistemich, Phys. Lett. **B230**, 21 (1989).
[96] Y. X. Luo, J. O. Rasmussen, I. Stefanescu, A. Gelberg, J. H. Hamilton, A. V. Ramayya, J. K. Hwang, S. J. Zhu, P. M. Gore, D. Fong, E. F. Jones, S. C. Wu, I. Y. Lee, T. N. Ginter, W. C. Ma, G. M. Ter-Akopian, A. V. Daniel, M. A. Stoyer, and R. Donangelo, J. Phys. G: Nucl. Part. Phys. **31**, 1303 (2005).
[97] Y. X. Luo, J. H. Hamilton, J. O. Rasmussen, A. V. Ramayya, I. Stefanescu, J. K. Hwang, X. L. Che, S. J. Zhu, P. M. Gore, E. F. Jones, D. Fong, S. C. Wu, I. Y. Lee, T. N. Ginter, W. C. Ma, G. M. Ter-Akopian, A. V. Daniel, M. A. Stoyer, R. Donangelo, and A. Gelberg, Phys. Rev. C **74**, 024308 (2006).
[98] R. Schneider, Ph.D. thesis, Technische Universität München, 1996.
[99] A. Stolz, Ph.D. thesis, Technische Universität München, 2001; http://deposit.d-nb.de/cgi-bin/dokserv?idn=962132349.